Optics & Laser Technology 192 (2025) 113762

Contents lists available at ScienceDirect

Optics and Laser Technology

journal homepage: www.elsevier.com/locate/optlastec

Full length article

Effects of laser beam shaping on Ti-6Al-4V single tracks in PBF-LB/M: A study with Aconity MIDI+

Abid Ullah [a,b,c,*], Ahmad Reshad Bakhtari [d], Alexander E. Medvedev [a], Andrey Molotnikov [a], Dirk Herzog [c,e], Ingomar Kelbassa [c,e], Claus Emmelmann [b], Milan Brandt [a,**]

[a] Centre for Additive Manufacturing, School of Engineering, RMIT University, Melbourne, VIC 3000, Australia
[b] Institute of Laser and Systems Technology, Hamburg University of Technology, D-21079 Hamburg, Germany
[c] Institute for Industrialization of Smart Materials, Hamburg University of Technology, D-21079 Hamburg, Germany
[d] Warwick Manufacturing Group, University of Warwick, Coventry CV4 7AL, United Kingdom
[e] Fraunhofer IAPT, D-20129 Hamburg, Germany

ARTICLE INFO

Keywords:
Additive manufacturing
Laser powder bed fusion
Beam shaping
Ti-6Al-4V

ABSTRACT

The application of beam shaping is gaining increasing interest in laser-based additive manufacturing (AM) technologies, as it revolutionizes the process by providing additional control over incident energy distribution and the resultant microstructure and mechanical properties of the manufactured part.

This study provides a comprehensive analysis of how different laser beam profiles (Mode 0, Mode 3, Mode 6), applied via the Aconity MIDI+ system, in combination with varied layer thicknesses (30 μm, 60 μm, and 90 μm) and linear energy inputs (up to 1.0 J/mm), influence single-track formation, surface morphology, roughness, and melt pool behavior in the Laser Powder Bed Fusion (PBF-LB/M) process of Ti-6Al-4V, offering new insights essential for process optimization. To further elucidate these effects, a complementary FEM model was used to analyze how beam shape affects melt pool dynamics and overall process stability. The findings reveal that transitioning from a conventional Gaussian beam (Mode 0) to a ring-shaped beam (Mode 3 and Mode 6) promotes conduction-mode melting, resulting in enhanced process stability and smoother melt track formation at higher linear energy densities. These beam profiles reduce certain defects, including spattering and balling, while producing wider and more stable melt tracks. Conversely, Mode 0 generates deeper melt pools, increasing the likelihood of keyholing and tracks surface roughness at elevated energy levels. While a thinner layer (~30 μm) facilitates stable and smoother track formation across all beam profiles, thicker layers (≥60 μm) exacerbate surface roughness and defects, especially with Mode 0. In contrast, the ring-shaped beams produce wider, smoother, and more stable melt tracks at higher energy inputs (~0.6–1.0 J/mm) with thicker layers. These insights are particularly valuable for high-performance applications in aerospace and biomedical industries, where precise control over surface quality and defect formation in Ti-6Al-4V components is essential for meeting certification standards and ensuring production efficiency. Overall, these findings highlight the critical role of beam shaping, layer thickness, and energy input in achieving stable melt tracks and improving the consistency and reliability of the PBF-LB/M process.

1. Introduction

Powder Bed Fusion of Metals using a laser-based system (PBF-LB/M) has emerged as a key additive manufacturing (AM) technique, gaining increasing interest in industries such as aerospace and automotive for producing complex metallic components. However, several barriers still prevent its widespread industrial adoption despite significant advancements and proven applications [1–3]. Among the most critical challenges are the lengthy manufacturing time [4,5], structural defects, and the uncertain quality of the finished products [6–8]. The part defects can severely deteriorate the microstructure and physical properties of a material, resulting in degraded strength and fatigue performance of the

* Corresponding author at: Centre for Additive Manufacturing, School of Engineering, RMIT University, Melbourne, VIC 3000, Australia.
** Corresponding author.
E-mail addresses: abid.ullah.ism@tuhh.de, abidmech95@gmail.com (A. Ullah), milan.brandt@rmit.edu.au (M. Brandt).

https://doi.org/10.1016/j.optlastec.2025.113762
Received 20 March 2025; Received in revised form 7 July 2025; Accepted 13 August 2025
Available online 23 August 2025

parts [9,10]. While the PBF-LB/M process has the potential to achieve near-full density in parts by utilizing a laser source that involves rapid thermal cycles of heating, cooling, and solidification [11–13], these same thermal fluctuations can also introduce complex microstructural behaviors, leading to defects that impact the final product's performance. To produce parts with controlled or minimized part defects and desired properties, it is necessary to understand the relationship between process parameters and key experimental factors such as melt pool stability, layer-wise melting behavior, and the formation of certain defects, including surface roughness, spattering, and balling, as well as their influence on the final part quality. In PBF-LB/M research, researchers have mainly focused on optimizing process parameters like laser power, scan strategy, hatch distance, and scan speed [14–17], but there has been comparatively less attention on investigating the effects of laser beam shaping (LBS) in conjunction with variations in key laser parameters and powder layer thicknesses.

The beam profile or beam shape refers to the spatial distribution or intensity of the laser beam over its cross-section. In other words, beam shaping is defined as the redistribution of irradiance and phase in a beam of optical radiation, controlling how energy is delivered to a target to achieve a specific intensity distribution [18]. Most of the commercial PBF-LB/M machines use a Gaussian beam shape for laser intensity and surface irradiation [19,20]. However, the traditional Gaussian beam shape has intrinsic limitations that might affect the quality and properties of the end product. The peak intensity at the center of the beam profile rapidly increases the temperature of the material from solid to vaporization in a matter of milliseconds. The Gaussian peak intensity in PBF-LB/M imposes limitations on the process window by causing keyholing evaporation, balling, and spatter generation. It also induces large thermal gradients and high solidification rates, leading to potential defects at elevated laser power and lower scanning speed [20–22]. Studies have shown that beam shaping plays a critical role in optimizing heat distribution, process stability, and track quality, ultimately impacting productivity, final part quality, and build performance [23–27]. The use of LBS in laser welding began in the 1990s and has grown significantly in the past two decades [28,29]. Studies in laser welding have identified beam shaping as a potentially effective method to address challenges related to low weld rates, process efficiency, and overall surface roughness. Previous literature, particularly in laser welding, emphasizes that LBS offers a number of benefits such as improved process stability, a widened process window, and reduced defects [30,31]. Additionally, it contributed to tailoring the microstructure, improving corrosion resistance, and increasing hardness [32–35]. However, there is still a notable gap in research on the effects of beam shaping in laser AM, as indicated by the limited available literature on LBS in the PBF-LB/M [23,24,26]. This scarcity in the publications implies that there is a large unexplored area for this kind of research for future investigation.

So far, Top-hat, Donut, Elliptical, Gaussian, and Bessel beam forms have been studied to some degree in PBF-LB/M. The normalized intensity distributions of these beam profiles are illustrated in Fig. 1 for visual comparison. In their study on PBF-LB/M of AlSi10Mg, Wischeropp et al. [36] demonstrated that a Donut-shaped beam resulted in wider but shallower melt pools compared to its Gaussian counterpart under identical processing conditions. Their findings revealed that the Gaussian beam produced melt pools approximately 30 % deeper, suggesting that higher laser power ($>$ 400 W) is required to achieve full densification with Donut beam shapes. Similarly, Loh et al. and Sow et al. [37,38] conducted comparative studies on Gaussian and Top-hat beam profiles in the PBF-LB/M of aluminum alloy 6061, highlighting that the Top-hat beam significantly increased melt pool width while exerting minimal influence on depth. Tenbrock et al. [39] further examined keyhole and conduction mode melting using Top-hat profiles under constant layer thickness and recommended further exploration of layer thickness effects on melt pool dynamics. Additionally, Okunkova and Gusarov et al. [37,40,41] explored the influence of Gaussian, Top-hat, and Donut beam shapes on Co-Cr alloy, revealing those non-Gaussian profiles, particularly Top-hat and Donut, enhanced process stability and productivity. However, the previous studies on beam shaping in PBF-LB/M largely focused on a limited range of materials and primarily investigated the spattering effects and production rates, leaving gaps in understanding the broader implications of beam shaping. To ensure high-quality PBF-LB/M-fabricated components, selecting an appropriate beam profile alongside optimized process parameters is critical for achieving the desired microstructure and surface quality with minimal defects. Ti-6Al-4V, a widely used $\alpha + \beta$ titanium alloy in aerospace, biomedical, and automotive applications, offers a

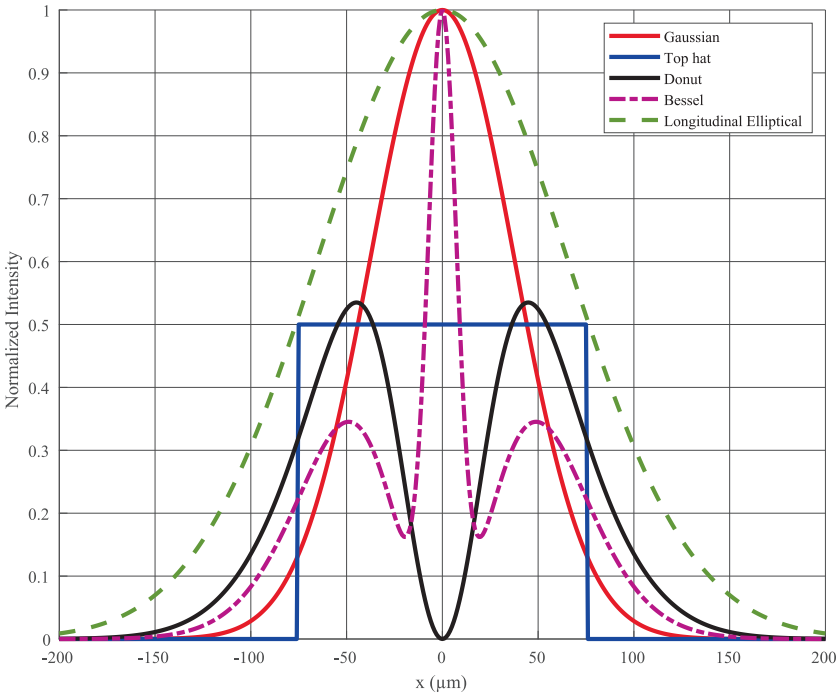

Fig. 1. Normalized intensity profiles of common laser beam shapes used in PBF-LB/M.

balance of strength and ductility due to its dual-phase microstructure [42,43]. While numerous studies have examined PBF-LB/M of Ti-6Al-4V, focusing on parameters such as laser power, scan speed, hatch spacing, and layer thickness in relation to microstructure and mechanical properties [44,45], the specific effects of LBS on this material remain unexplored. Since beam shaping is still in the early stages of research, analyzing track formation provides key insights into process optimization [46,47]. This method facilitates expanding the processing window and refining parameters for improved manufacturability. However, the influence of alternative beam shapes on melt track formation, stability, melt pool characteristics, and process efficiency remains insufficiently understood. To address this, the present study systematically investigates the effects of three distinct laser beam profiles under varying laser energy inputs and layer thicknesses, providing a comprehensive understanding of how these factors interact to shape track morphology and process stability for Ti-6Al-4V components.

2. Experimental procedure

2.1. Material and equipment

The experiments were conducted using gas-atomized Ti-6Al-4V (Grade 5) powder (ECKART TLS GmbH, Germany), featuring a predominantly spherical morphology. The particle size distribution ranged from 15 to 45 μm, with D10 = 26.72 μm, D50 = 37.93 μm, and D90 = 50.18 μm. The AM setup employed in this study utilizes a PBF-LB machine, the Aconity MIDI+ (Aconity3D GmbH, Germany), managed through AconitySTUDIO, a web-based control software. The laser source is an nLIGHT multi-mode laser, with a power of up to 1200 W. The optical setup includes an F-Theta lens with a standard spot size of 130 μm, adjustable between 130 μm and 500 μm for 3D scanning. The AFX fiber laser allows modulation from a full Gaussian beam (Mode 0) to a ring mode (Mode 6) through five intermediate modes, where higher modes concentrate more power on the beam edge, increasing the minimum spot size. In this work, Mode 0 (edge-to-core power ratio is E:C = 00:100, equivalent to pure Gaussian mode), Mode 3 (E:C = 54:46) and Mode 6 (E:C = 89:11), were used as shown in Fig. 2.

2.2. Design of experiments

In addition to LBS, this study varied laser and scan-related parameters, including laser power (150–250 W), scan speed (250–650 mm/s), and layer thickness (30, 60, and 90 μm) to evaluate their influence on track properties. A One Factor at a Time (OFAT) approach was employed, in which one parameter was varied per experiment while the others were held constant. This method allows clear attribution of changes to individual variables and is particularly effective for early-stage process window development when working with a limited number of experiments [48].

A total of 27 single tracks were fabricated for each LT on a single Ti-6Al-4V plate at room temperature, resulting in 81 single tracks across three plates, with variations in beam shape, laser power, and scan speed. A top view of a build plate along with the schematic illustration is shown in Fig. 3. Each single track had a length of 50 mm, with a 2 mm spacing between adjacent tracks. The linear energy density (LED, E_l) was calculated using equation (1), resulting in values ranging from 0.237 J/mm to 1.00 J/mm. Similarly, areal energy density (AED, E_a) was determined using equation (2), resulting in values between 1.78 J/mm^2 to 7.69 J/mm^2. The various combinations of laser power and scanning speed used for printing the single tracks are detailed in Table 1.

$$E_l = \frac{P}{v} \tag{1}$$

$$E_a = \frac{P}{D.v} \tag{2}$$

where P is the total laser power (W), v is the scanning speed (mm/s), and D is the laser beam diameter (mm) measured for each beam shape.

2.3. Characterization

The overall quality, surface roughness, and melt pool geometries of the single melt tracks were analyzed using a 3D Laser Scanning Confocal Microscope VK-X160K from Keyence. The top surface roughness (*Ra)* of the single tracks was calculated using a horizontal two-point multi-lines approach by the Keyence MultifileAnalyzer software. A Zeiss Supra 55 VP Field Emission Gun Scanning Electron Microscope (FEG-SEM) was also used for surface analysis and melt pool geometries. Additionally, surface imaging was performed using a Keyence VHX-7000 Digital Microscope, which provides high-resolution imaging with optical shadow effect mode. Following detailed 2D and 3D surface morphology analysis and surface roughness measurements, the plates were sectioned into smaller specimens using a high-speed diamond wheel, with each specimen containing three single tracks for final analysis. The cross sections of the samples were embedded using a Buehler SimpliMet Metallurgical Mounting Press and subsequently ground (P320-P4000) as well as polished with 9 μm and 3 μm diamond suspension using the Struers Rotopol-31 base with Rotoforce-4 polishing head. Finally, the samples were polished using the VibroMet2 vibration polisher for up to six hours with a MasterMet-2 non-crystallizing colloidal silica polishing suspension. To reveal the melt pool geometry, the samples were etched with Kroll solution which consists of 5 % nitric acid (HNO3) and 2 % hydrofluoric acid (HF) in water. The width, depth, and height of the melt pool were measured using the Keyence MultifileAnalyzer software. Fig. 4 shows an illustrative example of the measurement and assessment method for each melt pool of the single tracks. Additionally, track width was measured at five different locations along each single track using the Keyence software, and the average value was calculated to ensure accurate quantification across different processing conditions. Fig. 5 presents a visual classification of representative single tracks, illustrating a

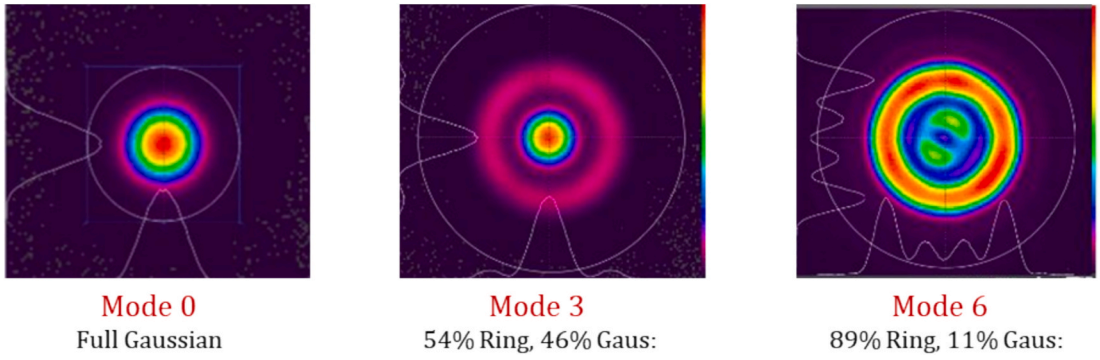

Fig. 2. Near-field images of beam profiles at Modes 0, 3, and 6 used in the experiments (courtesy of Aconity GmbH).

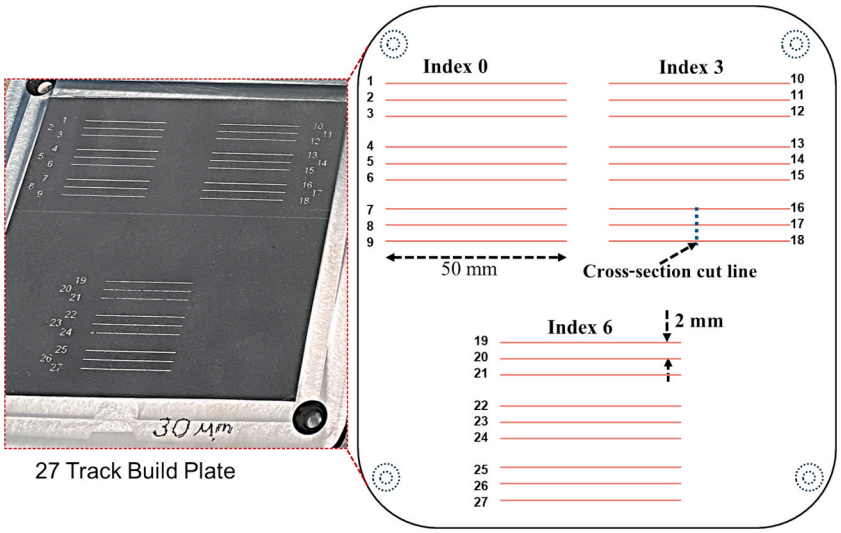

Fig. 3. Top view image of one of the three 27 track build plates and its schematic illustration used in this study.

Table 1
Parameters for single melt track experiments.

Beam Profile	Nominal Spot diameter *Ø (μm)*	Laser power *(W)*	Scan speed *(mm/sec)*	Layer thickness *(μm)*	LED Range (J/mm)	AED Range (J/mm^2)
Mode 0	135	150, 200, 250	250, 450, 650	30, 60, 90	0.023–1.0	1.77–7.69
Mode 3	210	150, 200, 250	250, 450, 650	30, 60, 90	0.023–1.0	1.15–4.76
Mode 6	383	150, 200, 250	250, 450, 650	30, 60, 90	0.023–1.0	0.60–2.611

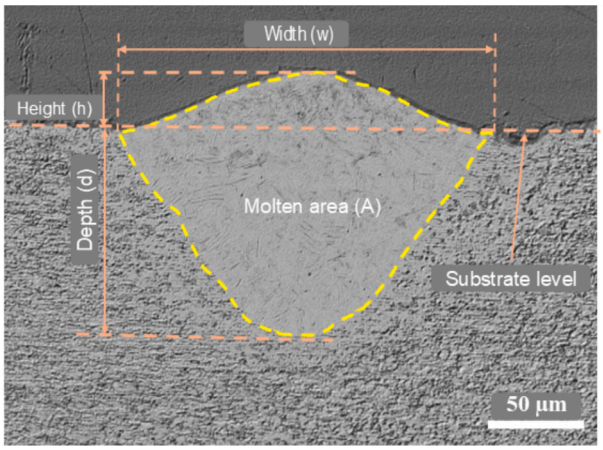

Fig. 4. Cross-sectional view of a single laser track, depicting key melt pool characteristics.

variety of morphologies based on top-view continuity, magnified surface features, profile graphs, and cross-sectional geometry. This classification highlights a spectrum of track conditions, from unstable cases exhibiting balling and discontinuities to relatively stable and fully continuous formations. Although the surface profile graphs were not quantitatively analyzed in the results section, they are included to provide qualitative insight into track width distribution and surface structure. The full analysis and discussion are presented in Section 3.1.

2.4. Numerical analysis

A continuum-based thermal model was developed to investigate the impact of different laser beam shapes (Mode 0, Mode 3, and Mode 6) on the formation of single tracks in the PBF-LB/M process. The powder layer, though inherently discrete, is treated as a continuum with equivalent thermophysical properties, ensuring an accurate representation of its thermal response. A domain of 2.5 × 1 × 0.03 mm and a 2.5 × 1 × 1 mm is considered for the powder layer and substrate, respectively (see Fig. 6). A symmetry boundary condition is imposed on the plane y = 0.5 mm to reduce computational effort. The model incorporates temperature-dependent material properties [49,50] to capture and accurately represent the evolving behavior of the Ti-6Al-4V alloy during the PBF-LB/M process with precision including the phase change from powder to solid. The thermophysical properties of the material are listed in Table 2, with values outside the specified ranges linearly extrapolated.

The temperature (T) in the single-track model is simulated by solving the heat balance equation:

$$\rho C_p \frac{\partial T}{\partial t} + \rho C_p u \nabla T = \nabla(k \nabla \mathrm{T}) + Q(x,y,z) \tag{3}$$

where (ρ) density, (C_p) specific heat capacity, (k) thermal conductivity, (u) laser velocity, and ($Q(x,y,z)$) heat source. An exponentially decaying volumetric heat source, adapted from [51,52], is used and modified to accommodate different beam shapes (i.e., Mode 0, Mode 3, and Mode 6) (Fig. 7):

$$Q(x,y,z) = \left[\frac{\beta AP}{\pi\delta\omega^2}\exp\left(-\frac{r^2}{\omega^2}\right) + \frac{(1-\beta)AP}{4\pi\delta R\omega_r} exp\left(\frac{-(r-R)^2}{\omega_r^2}\right)\right]\exp\left(-\frac{|z|}{\delta}\right) \tag{4}$$

A is the absorption coefficient used to calibrate the model, β is the intensity splitter between the central Gaussian distribution and the outer ring distribution, P is laser power, r is a function for the coordinates of the beam center, ω is central Gaussian spot radius, ω_r is ring Gaussian distribution radius, R is ring radius, $|z|$ is the absolute value of the z-coordinate, and δ is laser optical penetration depth, which is taken equal to 0.03 mm for Ti-6Al-4V.

The initial condition assumes the entire domain is at ambient tem-

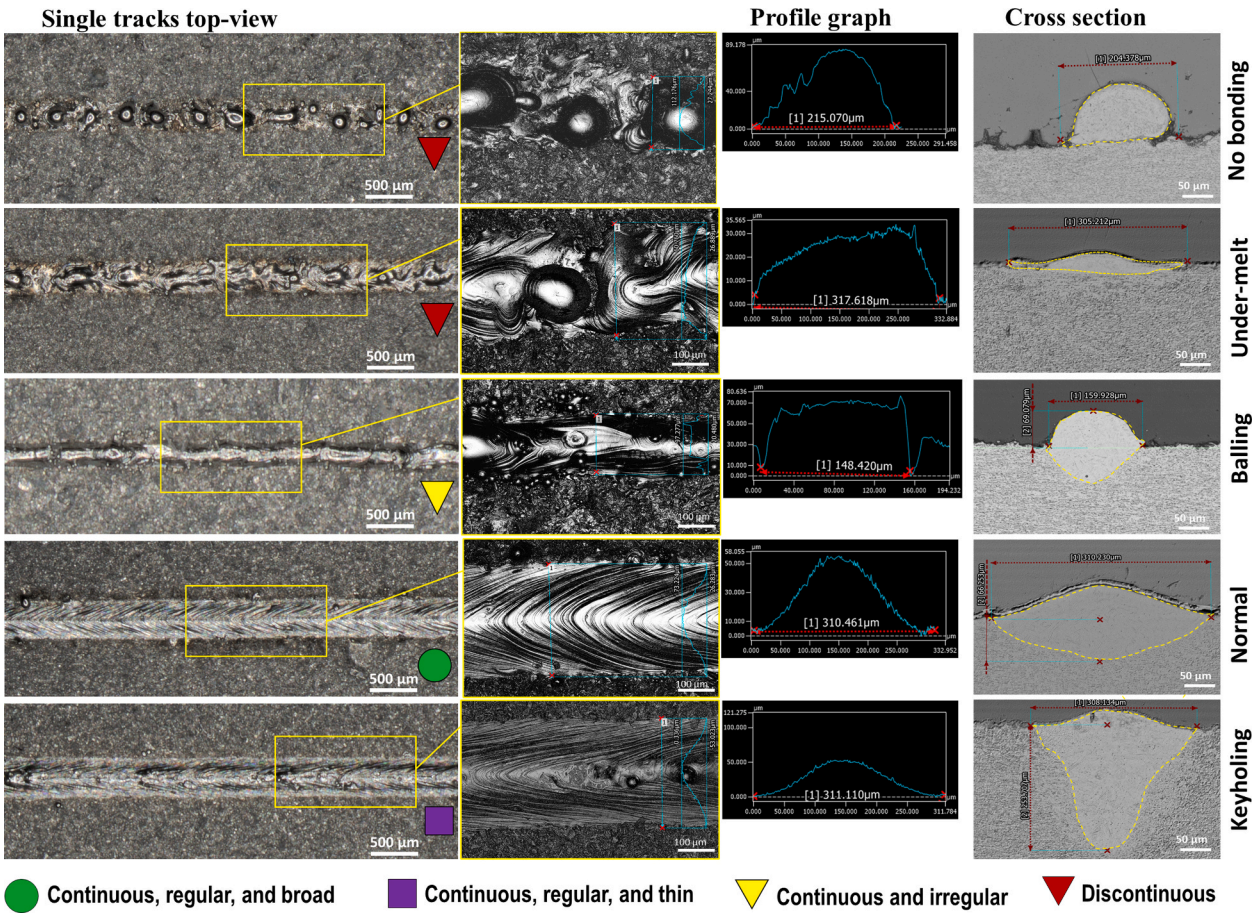

Fig. 5. Classification of single tracks based on surface continuity, width, and defect formation, alongside classification of melt pool types according to their size, shape, and stability characteristics across different processing conditions.

perature (i.e., $T_0 = 293$ K at $t = 0$), and a heat loss due to convection and radiation at the top surface of the domain takes place during the laser and material interaction and can be expressed as follows:

$$-k\frac{\partial T}{\partial n} = h_c(T - T_0) + \varepsilon\sigma(T^4 + T_0^4) \tag{5}$$

The (−) sign shows the heat loss from the domain surface (n), h_c is the convective heat transfer coefficient, ε is the surface emissivity coefficient, and σ is the Stefan-Boltzmann constant.

The phase change is modeled via the apparent heat capacity method [53], whereby the latent heat is incorporated as an additional contribution to the specific heat capacity:

$$\rho = \theta\rho_{solid} + (1-\theta)\rho_{liquid} \tag{6}$$

$$C_p = \frac{1}{\rho}(\theta\rho_{solid}C_{p,solid} + (1-\theta)\rho_{liquid}C_{p,liquid} + L\frac{da}{dT} \tag{7}$$

$$k = \theta k_{solid} + (1-\theta)k_{liquid} \tag{8}$$

$$a = \frac{(1-\theta)\rho_{liquid} - \theta\rho_{solid}}{\theta\rho_{solid} + (1-\theta)\rho_{liquid}} \tag{9}$$

$$f(x) = \begin{cases} 0, if T \le T_S \\ \dfrac{T - T_L}{T_L - T_S}, if T_S < T < T_L \\ 1, if T \ge T_L \end{cases} \tag{10}$$

The phase fraction, θ, defines the state of the material ($\theta = 0$ for solid, $\theta = 1$ for liquid, with intermediate values representing a mushy zone). L represents the latent heat, and T_L and T_S represent the liquidus and solidus temperatures of the material, respectively. To accurately capture the temperature profile the domain is meshed with two distinct mesh settings (i.e., fine and coarse) using linear tetrahedral elements. A fine mesh with an element size of 0.0135 mm is considered for half of the powder layer and the substrate beneath it with a depth of 3 times the layer thickness and a coarse mesh with an element size of 0.25 mm for the rest of the domain (see Fig. 6). Finally, the commercial FEM software, COMSOL Multiphysics 6.2, is used to perform the thermal analysis with standard solver settings.

3. Results and discussion

3.1. Single-track morphology and formation dynamics

The influence of different beam shapes, layer thickness (LT), and linear energy density (LED) on the surface morphology and formation characteristics of single tracks is examined in this section. The results are categorized into three sets based on LT values of 30 µm, 60 µm, and 90 µm. Representative single tracks from the first set, produced at an LT of 30 µm, are shown in Fig. 8. For a clear comparison, the tracks are classified based on their morphology and formation stability into four categories. Stable tracks are continuous, uniform, and free from significant defects. Relatively stable tracks exhibit minor irregularities, such as slight waviness or occasional spattering, while still maintaining overall continuity. In contrast, unstable tracks display severe instabilities, including discontinuity, fragmentation, balling, and droplet formation, which indicate process uncertainty caused by either overmelting or undermelting of the powder bed. Lastly, broader-span tracks

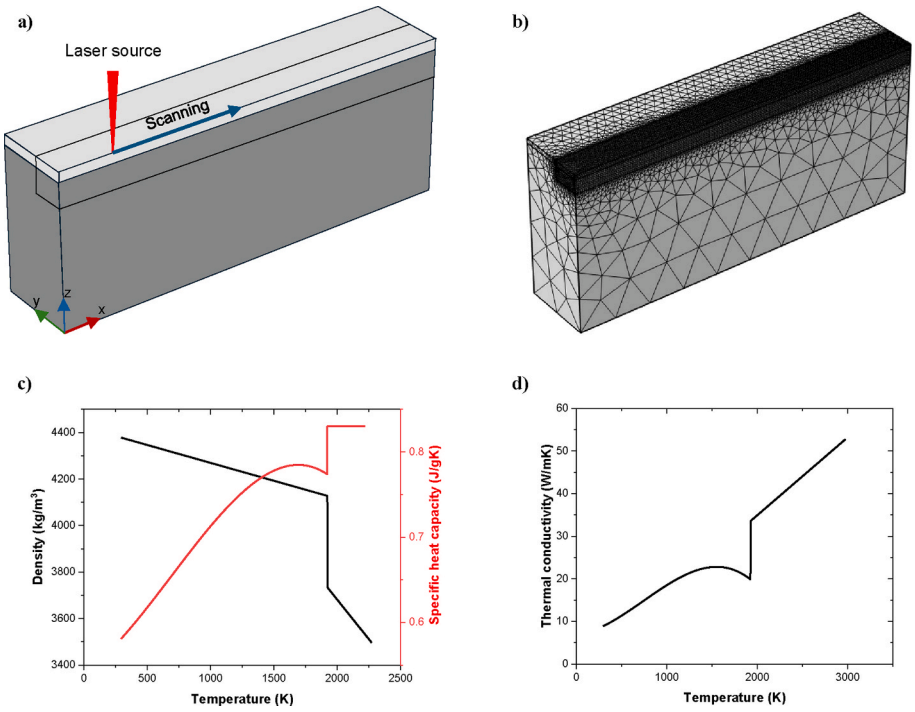

Fig. 6. (a) Schematic of the simulation domain, showing the laser source and scanning direction. The model consists of a powder layer on top a solid substrate. (b) Mesh configuration, with a refined mesh in the region of interest and a coarser mesh elsewhere. (c) Temperature-dependent thermophysical properties of Ti-6Al-4V: density (black) and specific heat capacity (red). (d) Temperature-dependent thermal conductivity of Ti-6Al-4V. (For interpretation of the references to color in this figure legend, the reader is referred to the web version of this article.)

Table 2
Thermophysical properties of Ti-6Al-4V [49,50].

Property	Value
Density (g/cm^3)	Fig. 6c
Specific heat capacity (J/gK)	Fig. 6c
Thermal conductivity (W/mK)	Fig. 6d
Emissivity (ϵ)	0.35
Coefficient of convective heat transfer	20 W/m^2*K
Optical penetration depth (δ)	One layer thickness (30 μm)
Latent heat of melting (L_f)	2.9*10^5 J/kg
Solidus temperature (T_s)	1878 K
Liquidus temperature (T_L)	1928 K

are characterized by increased width, typically resulting from higher laser energy input and a change in the beam shape, leading to enhanced lateral spread and improved track uniformity.

The tracks produced using beam shape Mode 0 with relatively low LED ($\leq$ 0.44 J/mm) are predominantly thin and asymmetrical, exhibiting deviations in direction and uniformity, along with surface imperfections such as droplets and uneven molten features. Despite these irregularities, the beam profile Mode 0 consistently produces continuous tracks, even at the lowest LED (~0.23 J/mm), as shown in Fig. 8(a). With a gradual increase in linear energy density to 0.66 J/mm, the tracks become stable, continuous, and regular compared to those at lower LED, with track width increasing from 186.3 μm to 294.2 μm. However, they still remain relatively thin and reveal spattering, with differences becoming more pronounced when compared to tracks produced using Mode 3 and Mode 6. In a study, Wang et al. [54] reported that thin and regular tracks form when the melt pool does not reach the vaporization

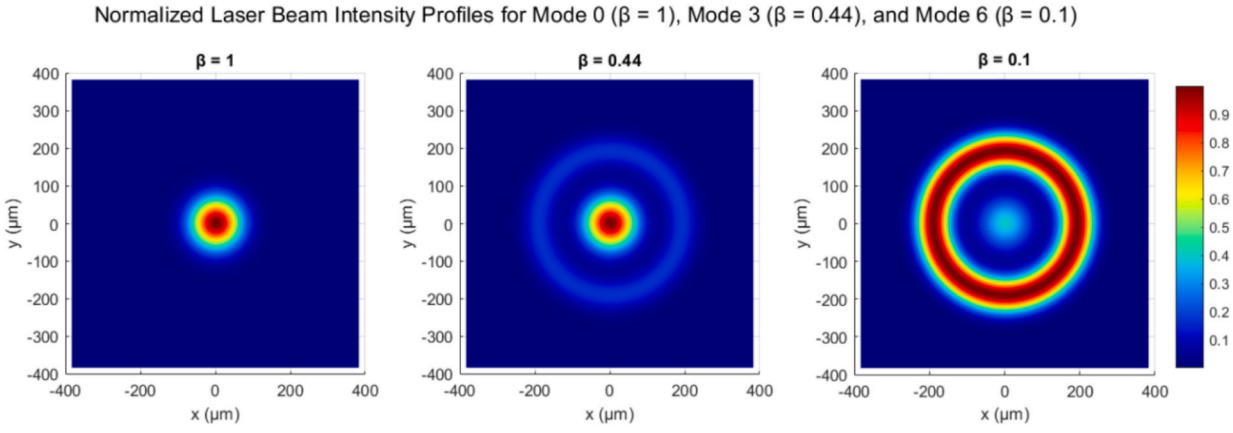

Fig. 7. Beam shape plots for the Mode 0 ($\beta = 1$), Mode 3 ($\beta = 0.44$), and Mode 6 ($\beta = 0.1$) using equation (4).

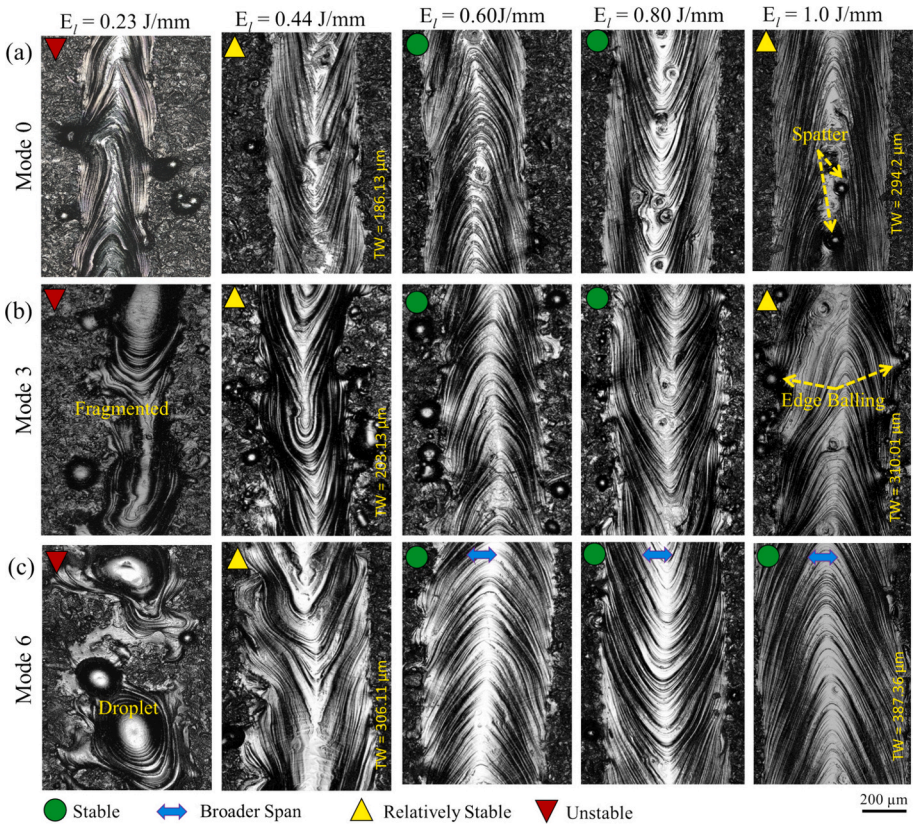

Fig. 8. Representative microscopic images of single tracks fabricated using different beam shapes (Mode 0, Mode 3, and Mode 6) at varying energy densities (0.23 J/mm – 1.0 J/mm) with a layer thickness of 30 µm.

point, preventing excessive powder displacement. In contrast, higher laser energy causes powder vaporization, leading to wider tracks and the formation of a powder-free zone using the Gaussian beam profile.

The single tracks produced with Mode 3 showed obvious irregularities and discontinuities, including fragmentation at the lower LEDs (0.23 J/mm to 0.44 J/mm) which were marginally improved by increasing the energy input to a moderate level (0.55 J/mm to 0.8 J/mm), as observed in Fig. 8 (b). However, tracks formed with Mode 6 at lower LEDs (< 0.44 J/mm) are observed to completely disintegrate, resembling balling, fragmentation, or distorted single tracks, as shown in Fig. 8(c). This behavior reflects the insufficient energy delivery for ring-shaped beam profiles, where the LED provided is not enough to ensure complete melting. The presence of fragmentation and discrete molten droplets indicates melt pool instability, with certain regions experiencing insufficient melting while others undergo excessive melting. The formation behavior of melt pools, which is correlated with these instabilities, is further analyzed in more detail in Section 3.3. Similar findings have also been reported in previous studies for various metal alloys [55,56]. Even at 0.44 J/mm, Mode 6 tracks still exhibit non-uniformity, necking, and fragmentation, suggesting process instabilities likely caused by insufficient energy input [57,58]. In contrast, using Mode 0 with the same lower LED produces relatively stable and continuous tracks free from balling, necking, or the formation of powder droplets along the track edges. At moderate to high energy densities (0.60 J/mm to 1.0 J/mm), all laser profiles produce continuous and relatively wider tracks compared to the lower LED levels (≤ 0.4 J/mm). Among these, Mode 0 generates some spattering at the center of the single tracks, whereas Mode 6 stands out for producing uniform, smooth, and significantly wider tracks, especially at higher energy input (1.0 J/mm).

The surface width of the tracks was precisely measured at five different points along each track, and the average values were calculated. The corresponding average track width measurements indicate that laser beam profiles significantly impact track width. Track width variations are closely linked to beam shape, beam diameter, energy density, and the overall uniformity of energy distribution. For clarity and ease of comparison, only the widths of single tracks produced at relatively lower and higher LEDs are labeled in Fig. 8, while Fig. 9 presents a comparative analysis of average surface track widths plotted against LED, providing further understanding of its relationship with beam shape and track formation. Reference lines indicating the nominal spot diameters (Ø) for each beam profile are included to assess how track width evolves relative to the beam size and to distinguish variations across different processing conditions. At lower LED values (<0.5 J/mm), track widths for all modes remain below or close to their respective spot sizes, whereas at higher LED (≥0.8 J/mm), Mode 0 and Mode 3 exhibit significant expansion beyond their nominal Ø, while Mode 6 remains constrained within its spot size. This confirms that beam shape influences track broadening, with Mode 6 ensuring lateral energy distribution and stable width, while Modes 0 and 3 exhibit increasing expansion with energy input. A notable increase of an average of 8.74 % in track width is observed when transitioning from Mode 0 to Mode 3. Mode 6 consistently produces the widest tracks across all energy levels, with a 22 % increase compared to Mode 0. At high LED levels (0.8–1.0 J/mm), track width increases uniformly across all beam profiles, with the most significant rise in Mode 6, where the average width reaches 387.36 µm. These single tracks are classified as broader and stable. Compared to the lower LED, track width increased by approximately 56 % for Mode 0, 59 % for Mode 3, and 63 % for Mode 6 at the higher energy density. These variations in track width trends align with the differences in melt pool expansion, which are further examined through areal energy density (E_a) in Section 3.4. Similar trends were found in a previous study for the single tracks of 316L/CuSn10 multi-material where lower energy input and insufficient wetting caused the formation of balling and

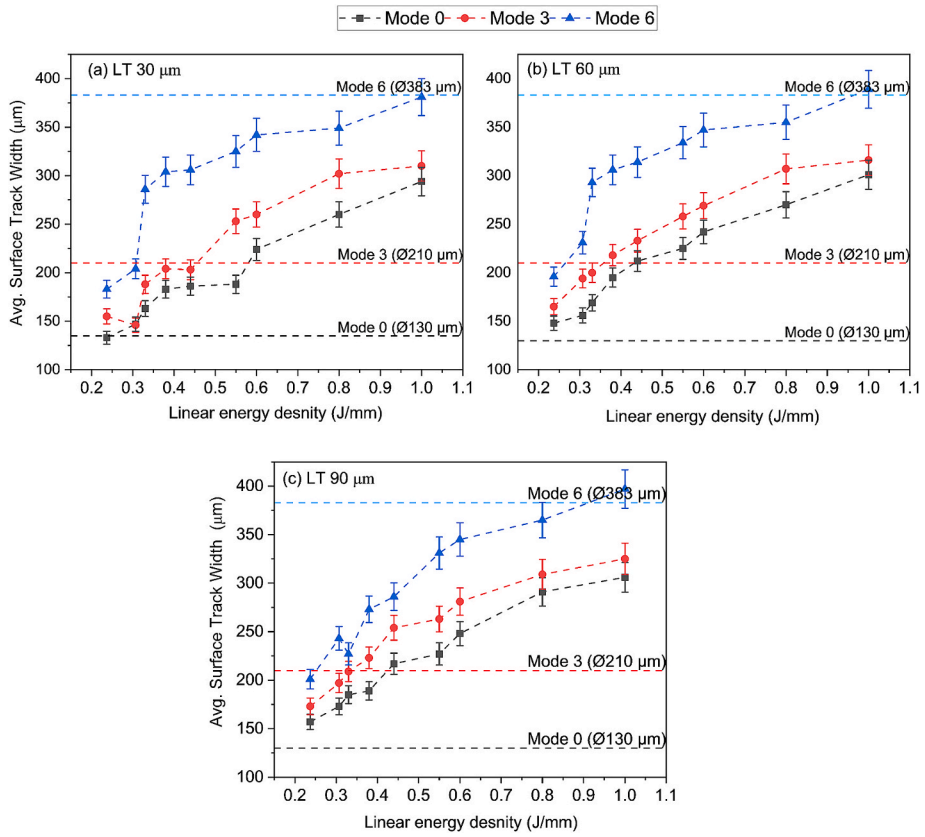

Fig. 9. Variation of average surface track width with linear energy density (LED) for different beam modes (Mode 0, Mode 3, and Mode 6) at three-layer thicknesses (LT): (a) 30 μm, (b) 60 μm, and (c) 90 μm.

discontinuity of tracks while a systematic increase in the width of the tracks was observed with the increasing laser power and reducing scanning speed [59].

When the LT increases to 60 μm and 90 μm, the overall track formation trends remain similar to those observed for the 30 μm layer. At lower LED, track instability is evident across all LTs. However, as LED increases, track stability improves consistently, regardless of the LT. In the case of Mode 0 with 60 μm LT, tracks exhibit an increased tendency to necking and a higher occurrence of edge instabilities such as balling and droplet accumulation at lower linear energy inputs. Additionally, more spatter is observed at the center of the melt pools at relatively higher energy densities (0.66 J/mm to 1.0 J/mm). The solidified melt pool ripples also appear less consistent, and the track edges become more irregular compared to the 30 μm layer. These variations are clearly illustrated in the supplementary data, Fig. S1. For the 90 μm LT (Supplementary Fig. S2), the tracks follow a comparable trend to the 60 μm layer but with marginally broader melt tracks. The average track width increases from 294.41 μm (30 μm layer) to 301.37 μm (60 μm layer), and further to 306.31 μm for the 90 μm layer at $E_l = 1.0$ J/mm, indicating a gradual widening effect with increasing LT, as illustrated in Fig. 9. However, the 90 μm tracks show more pronounced irregularities, including cracks, increased track discontinuities, and balling effects at lower energy densities, largely impacting the track stability, as illustrated by the color map in Fig. 10(c). Microcracks oriented perpendicular to the direction of single-track formation are also found on the track surfaces formed at lower LEDs (0.23 J/mm and 0.44 J/mm). Additionally, the tendency for necking and track drifting becomes more noticeable at lower to moderate LED levels (0.23 J/mm to 0.66 J/mm). These observed defects show the challenges associated with processing thicker layers.

For Mode 3, the primary differences with increasing LT include a noticeable widening effect, particularly at higher LEDs. The width of the tracks increases to 316.50 μm for the 60 μm LT and 325.09 μm for the 90 μm LT at the same $E_l = 1.0$ J/mm, as illustrated in Fig. 9 (b) and 9 (c) respectively, showing a significant enhancement compared to the 30 μm tracks. Besides, no significant changes are found for 60 μm LT at lower energy input (< 0.44 J/mm) under Mode 3 in comparison to LT 30 μm. However, the 90 μm LT exhibits a pronounced necking effect at the energy input of 0.44 J/mm, where localized narrowing of the melt track is observed. This highlights the increased track instability with thicker layers at lower LEDs, which may be attributed to the increased material volume requiring sufficient energy for sufficient melting. The tracks produced at 1.0 J/mm with the increased LTs are found to be comparatively wider, smoother, and more stable, whereas more edge instabilities were produced with the 30 μm LT. These tracks are categorized as "broader span" to highlight their comparatively greater width and stability, as also observed in Fig. 8 (c) for the 30 μm LT. For Mode 6, the tracks produced with thicker layers (60 μm and 90 μm) maintain their characteristic broader and more stable appearance, particularly at higher LEDs. A notable observation is the improved energy absorption across thicker layers, which results in more stable and wider (398 μm) track formation at higher energy levels (≥ 0.66 J/mm). These findings also confirm that LED variation has a more pronounced effect on track width compared to LT variation when using a shaped beam profile. Compared to Modes 0 and 3, Mode 6 exhibits greater track consistency, with fewer discontinuities and reduced surface defects at increased LTs (≥ 0.80 J/mm). This indicates that the broader energy distribution of Mode 6 is more effective for processing thicker layers, but only at higher LEDs, resulting in improved track formation and stability. Fig. 10 presents the single tracks stability map for comparisons.

The observed variations in single-track morphology and geometric features highlight the significant influence of LBS, LEDs, and LT on track formation. These parameters independently and collectively affect melt pool behavior, influencing track stability, defect formation, and

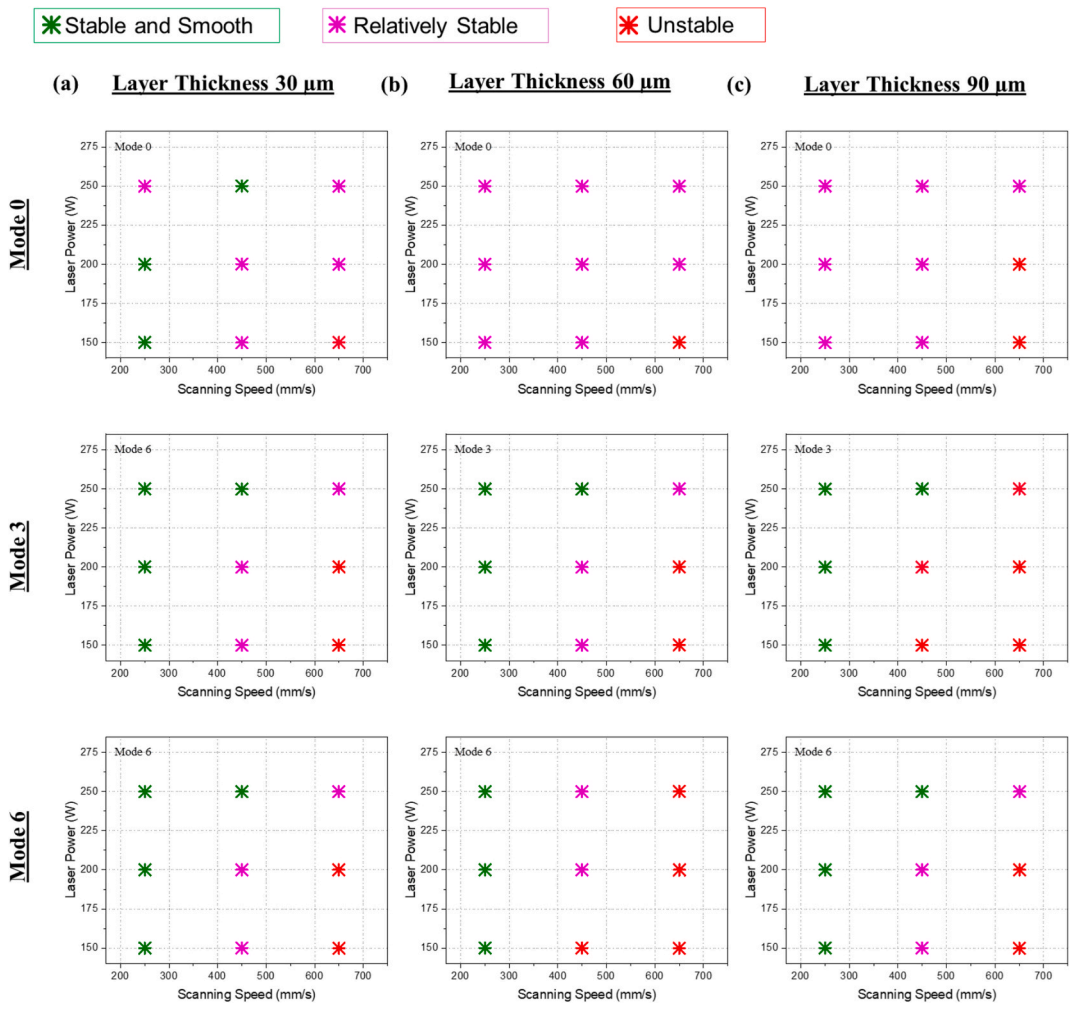

Fig. 10. Formation and surface stability map of single tracks fabricated using different beam shapes (Mode 0, Mode 3, and Mode 6) at varying laser power and scanning speeds across different layer thicknesses. For Mode 3, and Mode 6, stability is observed only when high LED (≥ 0.66 J/mm) is provided.

solidification dynamics [60,61]. Beam shape governs energy distribution over the melt pool, affecting its stability, while laser energy density controls melting extent and material fluidity, impacting track continuity and surface quality. LT influences heat accumulation and powder-bed interaction, further shaping melt pool behavior. The track continuity remained stable for Mode 0 at lower energy inputs due to its Gaussian profile, which concentrates energy at the center, creating a deep and defined melt pool. In contrast, Mode 3 and Mode 6 exhibited track fragmentation and droplet formation at lower LEDs, despite their more uniform energy distribution. This instability arises because a broader energy spread results in lower peak energy density, leading to insufficient localized heating, incomplete melting, and balling effects, as also observed by Wischeropp et al. [36,62] in AlSi10Mg with a ring beam profile. Additionally, central protrusions and edge depressions appeared at lower energy inputs, attributed to Marangoni-driven backward material flow [63] vaporization pressure, and Plateau–Rayleigh instability [64,65], where melt pool protrusions solidify and fragment into melt balls.

The findings also indicate that increasing LT worsens defects such as cracks, melt track drift, and edge instabilities, particularly with Mode 0. Thicker layers require higher energy input for complete melting, but improper adjustments can cause incomplete fusion or overheating, leading to increased thermal gradients and residual stress, which promote crack formation and melt pool instability [66,67]. In contrast, core-ring and ring-shaped beams offer a more uniform energy distribution, enhancing process stability and improving the handling of thicker layers. This reduces localized overheating and maintains consistent melt pool dynamics [25,68], resulting in wider and stable tracks even at higher layer thicknesses and laser energy inputs. These findings signify that utilizing a ring-shaped beam in the PBF-LB/M processing of Ti-6Al-4V can mitigate surface defects by providing a more uniform energy distribution, resulting in improved track stability and reduced issues such as cracks, deviations, and necking compared to Mode 0. It is worth to mention that the influence of spot size was not independently investigated, therefore, the wider melt tracks with Mode 6 may partly result from its larger spot diameter as well as its annular beam profile. Nonetheless, the results clearly show the combined effect of beam shape and process parameters on track stability, providing valuable insights for PBF-LB/M process control. In addition, the combination of higher LED (≥0.8 J/mm), higher LT, and the utilization of a ring-shaped appears to be an effective approach for producing wider melt tracks with enhanced stability. These wider tracks enhance build rates, and surface coverage, while reducing defects like incomplete fusion and porosity, as reported in previous studies [26,36].

3.2. Track top surface roughness

The variations in laser beam shape, energy density, and layer thickness directly impact track surface roughness, a critical quality attribute in PBF-LB/M. Surface roughness significantly influences the functional performance, mechanical properties, and post-processing requirements of the fabricated parts [69–71]. In particular, the

roughness of single tracks provides key insights into process stability, energy absorption, and defect formation, as also discussed in previous studies [72,73]. High roughness often correlates with unstable melt pools, spattering, and inconsistent energy distribution, affecting part quality and layer bonding. Fig. 11 illustrates these effects, highlighting the relationship between laser linear energy, beam shape, and track surface roughness. The primary contributors to increased track surface roughness include the formation of spatters, fragmentation, powder droplets, necking, and irregular ripples. These defects result from several undesired factors including unstable melt pool dynamics, vaporization, insufficient energy input, and non-uniform heat distribution, leading to irregular solidification and surface inconsistencies. The track surface roughness values exhibit a decreasing trend with increasing energy density for Mode 3 and Mode 6, whereas, for Mode 0, this initially decreases up to a critical threshold before growing again due to excessive energy input, which introduces process instabilities such as spattering and uneven solidification. At lower energy inputs ($\leq$ 0.4 J/mm), Mode 0 demonstrates relatively lower surface roughness primarily due to the continuity of the tracks and lower spattering effect. In contrast, at the same lower LED levels, Mode 3 and Mode 6 show relatively higher roughness values mainly due to incomplete melting and the formation of defects, as discussed in Section 3.1. However, a consistent reduction in surface roughness across all layer thicknesses is observed with increasing LED. This improvement is more pronounced in Mode 6, where uniform energy distribution facilitates stable melt pool formation and smoother track surfaces across all LTs. The plots in Fig. 11 (b) and 11(c) show that increasing LT from 30 μm to 90 μm amplifies surface roughness, especially in Modes 3 and 6 which is more obvious at lower LEDs. Previous studies [74,75] have also reported that increasing LT amplifies surface roughness challenges, primarily due to the increased material volume, which requires an adequate energy input to achieve uniform melting and prevent defects such as incomplete fusion and surface irregularities.

Fig. 12 presents high-magnification 3D microscopic images of the tracks with the 30 μm LT, providing further insight into the influence of beam shape, LED, and powder melting conditions on the surface quality of the melt tracks. The presence of spatter and balling is more dominant in tracks produced with Mode 0, becoming more pronounced with increased LED, as shown in the first row of Fig. 12(b). The high energy concentration in Mode 0 leads to evaporation and subsequent spattering, which is the primary cause of increased track surface roughness, as observed in Fig. 11 shows that at higher LEDs, Gaussian beams contribute to increased surface roughness, primarily due to evaporation, spattering, and keyhole formation at the beam's center. These effects introduce defects that degrade the surface quality of the melted layer [76–79], and the top surface of the track, as discussed in this study. The formation of these spatters significantly decreases when switching to Mode 3 and is further reduced or controlled by using Mode 6 at the same LEDs ($\geq$ 8 J/mm), resulting in smoother and more stable surface solidification, as shown in Fig. 12(b). The semi-circular wave-like features visible on the surface, often described as ripples, are indicative of how the material melts and flows under different beam profiles and energy inputs. These ripples, driven by surface tension forces from temperature gradients, impact melt pool surface roughness and ultimately affect overall part quality [57,80]. Mumtaz et al. [81] described that these forces arise from differences in temperature between the laser beam and the solidifying region, with thermal gradients, gravity, and melt pool curvature working to restore the surface; however, viscous forces and rapid solidification hinder complete relaxation [82]. While ripples contribute to surface roughness, they are inevitable due to the complex interactions between laser energy and the material, as well as oscillations in the molten pool during solidification. These findings indicate that beam shape has a significant influence on the formation of ripples. Mode 0 produces narrow and elongated ripples due to its concentrated energy profile, leading to smaller, deeper melt pools with steep thermal gradients that cause rapid cooling and localized heating [83], as observed in Fig. 12 under Mode 0. In contrast, tracks produced with Mode 3 and Mode 6 at higher LEDs exhibit broader, more uniform ripple patterns, confirming that ring-type beam shapes enhance melt pool stability and promote broader energy dispersion.

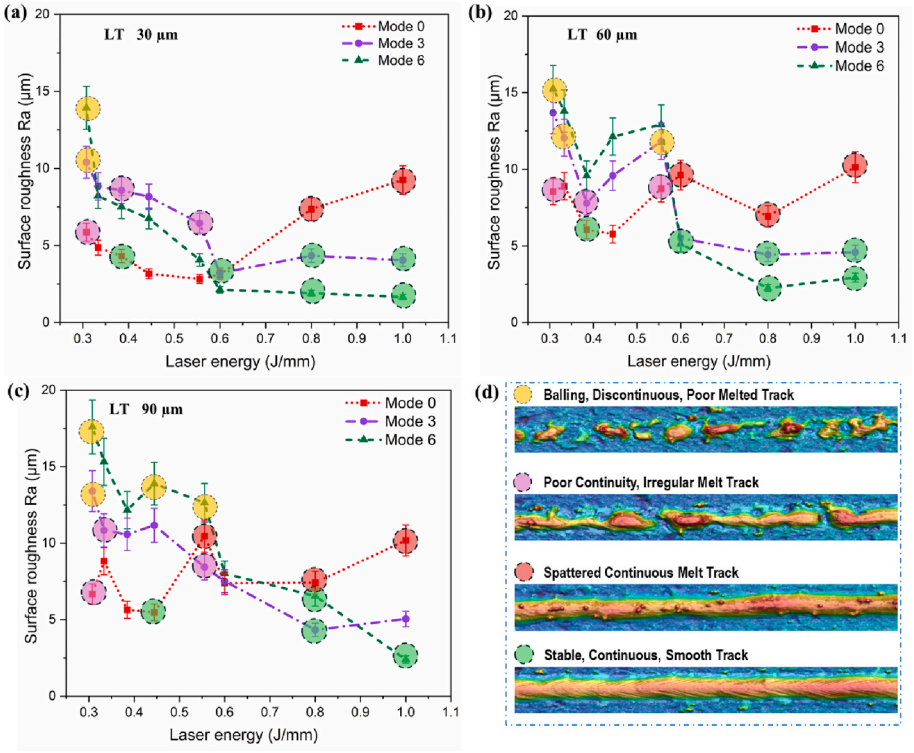

Fig. 11. Top surface roughness (*Ra*) of single tracks fabricated using different beam shapes (Mode 0, Mode 3, and Mode 6) at varying laser energy densities and layer thicknesses (LT): (a) 30 μm, (b) 60 μm and (c) 90 μm, (d) 3D surface topography images of representative tracks, highlighting the key sources of surface roughness.

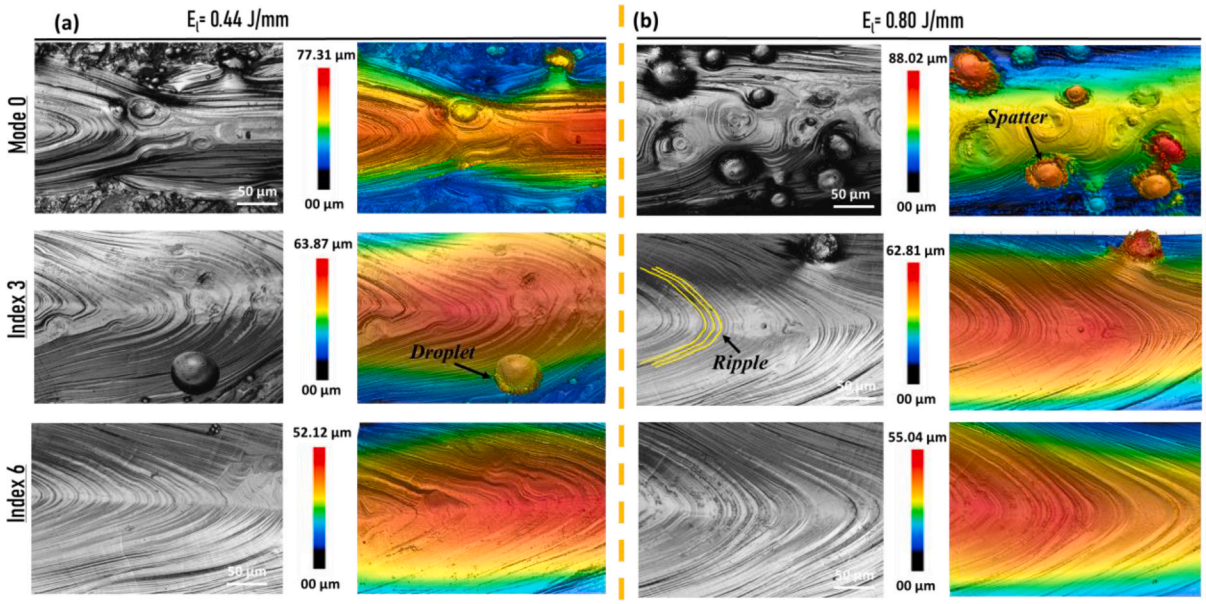

Fig. 12. 3D microscopic images of single tracks highlighting key surface features such as spatters, droplets, and ripples under different laser beam profiles and energy inputs (a) Comparatively lower LED (0.44 J/mm) (b) Higher LED (0.80 J/mm).

3.3. Melt pool characteristics

This section compares the effects of LBS, LT, and LED on melt pool width, depth, and height. The beam intensity profile influences temperature distribution, with peak temperatures typically occurring near the highest intensity region. The thermal field created by the laser beam determines the appearance and size of the melt pool. As the intensity of laser increases, it also increases the amount of vapor formed on the melted pool surface, which affects the recoil pressure. As recoil pressure increases, the processing conditions may shift from conduction to an intermediate phase (transition mode), and eventually to the keyhole mode [84,85]. The findings in this study reveal that LBS along with the variations in the LT and LED play an important role in determining the melt pool geometry, which in turn affects the microstructural characteristics and mechanical properties of the manufactured part [70–72]. Fig. 13 presents the cross-sectional melt pool geometries for the three laser beam shapes at varying LEDs and a constant LT of 30 µm. The trends in melt pool shape and size become more pronounced as the LED increases from 0.44 J/mm to 1.00 J/mm. The tracks produced with Mode 0 demonstrate a distinctive melt pool shape, with a pronounced depth and narrower width at lower LEDs. At a relatively lower LED of 0.40 J/mm, the melt pool is moderately narrow, with a depth of 81.03 µm and a width of 195.35 µm, indicative of concentrated energy deposition in a smaller region. The melt pool remains in transition mode up to 0.44 J/mm, where the width-to-depth (W/D) ratio stays between 2 and 3. With the increase of LED to 0.66 J/mm, the melt pool width expands

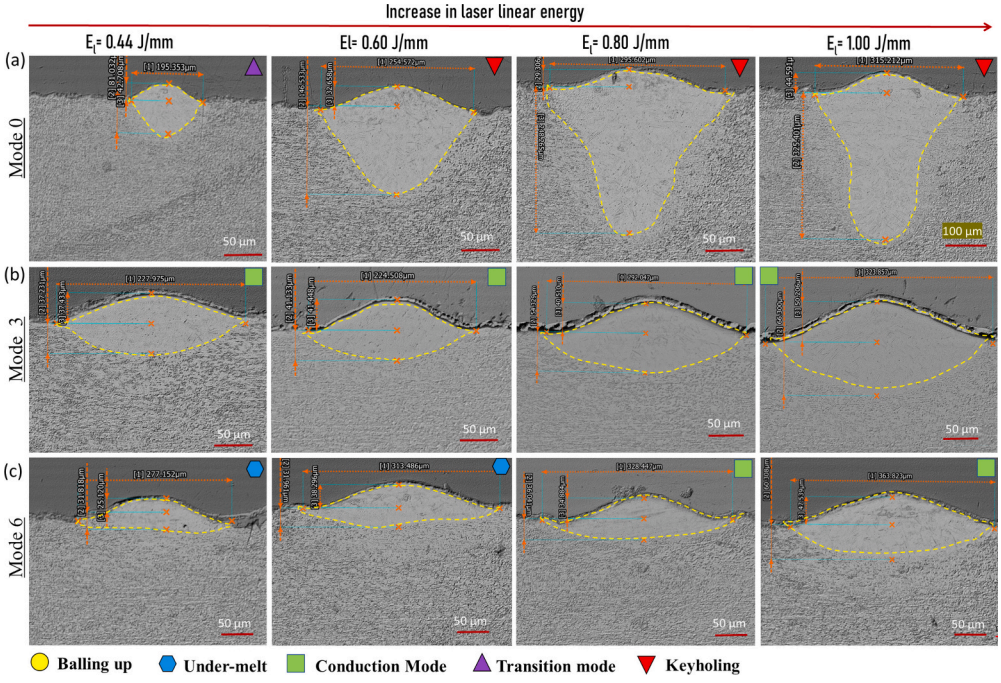

Fig. 13. Cross-sectional melt pool geometries for Ti6Al4V using three beam profiles (Mode 0, 3, and 6) at varying LEDs (0.40–1.00 J/mm) and LT 30 um.

to 254.572 μm, while the depth reaches 146.53 μm, and changes into keyholing (W/D < 2). A similar trend is observed with an increase in LED to 0.80 J/mm, resulting in a deeper melt pool of 248.25 μm with a slight increase in width, accompanied by the onset of keyholing. However, the melt pool reaches a maximum width of 315.21 μm and a significant increase in depth to 325.40 μm by increasing the LED to 1 J/mm, demonstrating the deeper penetration and keyholing of the laser with Gaussian beam profile at high energy input, as Fig. 13(a) confirms this trend. The quantified data of melt pool dimensions, including width, depth, and height, for different beam shapes and LT under varying energy densities, is plotted in Fig. 15, providing a comprehensive visualization of the trends and correlations discussed in this section.

'Mode 3 consistently produces a wider, shallower melt pool than Mode 0. At 0.44 J/mm, the melt pool width is significantly larger (~227.975 μm) than that of Mode 0, with a lower depth of 37.23 μm (W/D > 6), indicating a uniform energy distribution across the surface with smaller penetration. As the LED increases from 0.60 J/mm to 1.00 J/mm, the melt pool gradually widens and deepens, as seen in Fig. 13(b). However, the melt pools remain noticeably wider and shallower than those produced with Mode 0, indicating that Mode 3 provides a relatively stable melt pool geometry and maintains a balanced expansion in both width and depth. Mode 6 generates the widest but shallowest melt pools, with depths less than half of those in Mode 0 and Mode 3, as illustrated by the plots in Fig. 15 for Mode 6. This shows that ring-shaped beams produce exceptionally wider but less deep and shallower melt pools. The single melt tracks produced with lower LED (≤ 0.44 J/mm) exhibited insufficient penetration into the substrate, resulting in shallow and discontinuous profiles, which were categorized as under-melt melt pools. The simultaneous increase in the melt pool width at LED 0.44 J/mm, 0.60 J/mm, 0.80 J/mm, and 1 J/mm is noted as 227.15 μm, 313.48 μm, 328.44 μm, and 363.82 μm respectively, as also evidenced in Fig. 13 (c) under Mode 6 and respectively plotted in Fig. 15. This confirmed that the melt pools produced with Mode 6 are significantly wider compared to those produced with Mode 0 and Mode 3. Fig. 14 (a) shows a melt pool stability map providing an overview of the effect of beam shape, laser power, scan speed, LED, and LT on the melt pool formation and stability.

The findings confirm further that melt pool dimensions are significantly influenced by LT, LED, and LBS, with complex interdependencies. Increasing the LT to 60 μm results in a consistent increase in melt pool width, following a similar trend observed with the 30 μm layer. However, minor inconsistencies in melt pool depth and height indicate that greater LT introduces slight instabilities, particularly affecting the vertical dimensions of the melt pool. This also shows a strong correlation with the continuity of the single tracks, discussed in the previous section 3.1. The detailed figures depicting melt pool characteristics for the 60 μm LT are available in the supplementary data, Fig. S4. In the case of Mode 0, at relatively lower LED (0.44 J/mm), the melt pool width, depth, and height are measured as 209.12 μm, 101.75 μm, and 47.10 μm, respectively, which are larger than those produced with a 30 μm LT.

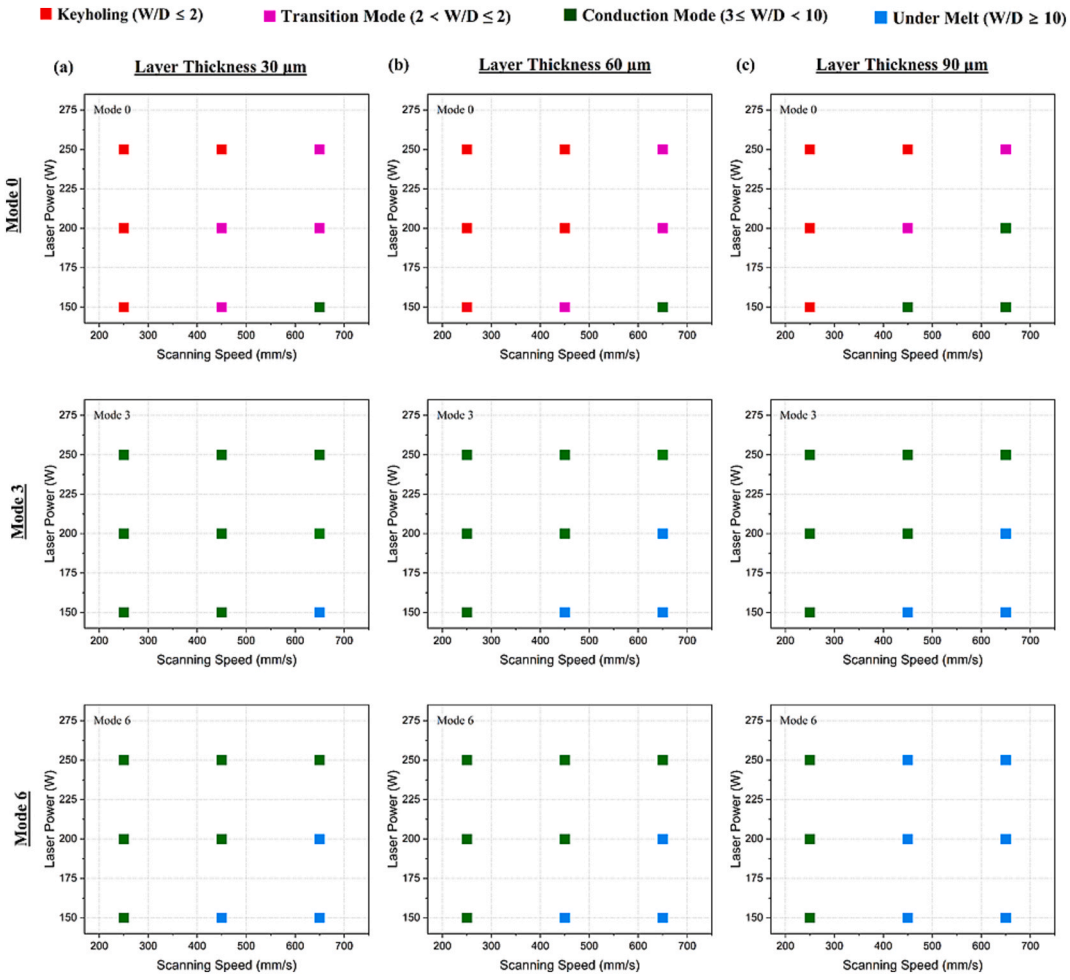

Fig. 14. Melt pool stability map showing the effects of laser beam shape (Mode 0, Mode 3 and Mode 6), layer thickness (30 μm, 60 μm, and 90 μm) and process parameters (laser power and scanning speed). Melt pools tend to remain unstable and exhibit keyholing behavior as energy density increases under certain conditions. Conversely, melt pool stability improves at higher energy densities achieved through increased laser power and reduced scan speed. Mode 6 resulted in relatively more under-melting at higher LT due to the lower applied LED.

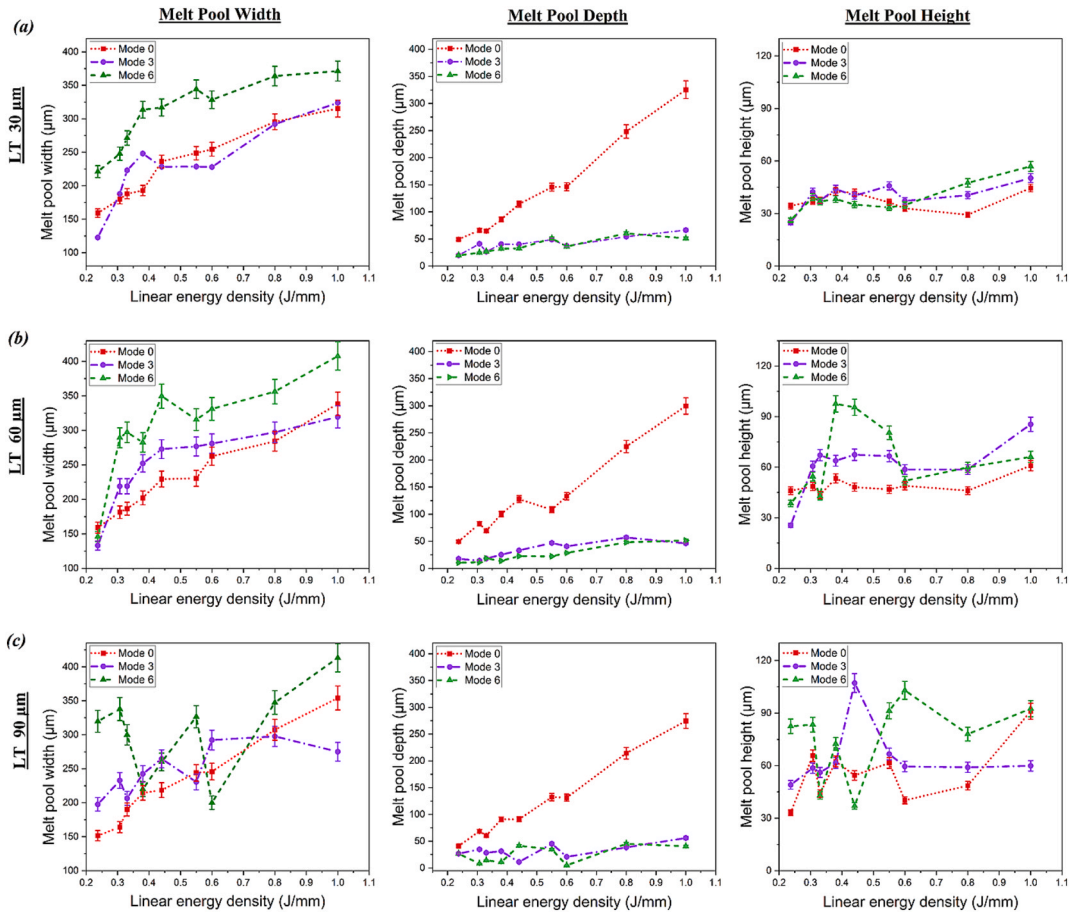

Fig. 15. Melt pool dimensions (width, depth, and height) for different beam shapes (Mode 0, Mode 3, and Mode 6) and layer thicknesses (LT) (a) 30 µm (b) 60 µm, and (c) 90 µm under varying laser energy densities (0.23 J/mm to 1.0 J/mm). Each subplot presents the measured melt pool geometry as a function of LED. Mode 0 typically produces deeper melt pools, while Mode 6 yields wider, shallower tracks. Melt pool height is more variable, especially at higher energy inputs and thicker layers.

This variation becomes more pronounced at higher LEDs (≥ 0.80 J/mm), where melt pool dimensions further increase due to enhanced energy absorption and the effect of enlarged LT at elevated energy levels. Mode 3 shows minimal changes in melt pool width relative to the 30 µm layer across both lower and higher LEDs. However, an increase in melt pool height is observed, with slight widening occurring at moderate energy levels (0.66 J/mm to 0.80 J/mm). The melt pools formed at energy density up to 0.44 J/mm exhibit characteristics of balling-up or poor layer bonding, where the melt pool width at the base exceeds the width of the upper bulge, as can be observed in Fig. S4 (b) in the supplementary data. This phenomenon indicates instability in melt pool formation, likely caused by insufficient laser energy input and surface tension effects, leading to incomplete fusion and track discontinuities. Bayat et al. [86] described the formation of a bulge of liquid metal at the center of the melt pool when using ring beam profiles, attributing this phenomenon to the absence of recoil pressure at the center of the ring beam. For Mode 6, a significant increase in melt pool height (up to 88.33 µm) is observed at lower energy density (≤0.44 J/mm), leading to the formation of protrusions that directly correlate with balling defects in the tracks. This also directly impacts track height, which can be further compared with the 3D single-track surface images in Supplementary Fig. S3. However, with increasing LED (≥ 0.8 J/mm), the melt pool stabilizes, resulting in a consistent increase in overall dimensions. The transition from balling and under-melt conditions to conduction mode is evident, demonstrating improved energy absorption and more uniform melting behavior, as illustrated in Fig. 14(b) under Mode 6.

For an LT of 90 µm (Supplementary Fig. S5), a comparatively wider melt pool with reduced depth but increased height is observed relative to the 30 µm and 60 µm layers. At lower energy input with Mode 0, the maximum measured melt pool dimensions are 213.14 µm in width, 84.57 µm in depth, and 69.01 µm in height at E_l = 0.44 J/mm. As LT increases, the width and height of the melt pool exhibit consistent growth, whereas the depth decreases. However, the changes in melt pool dimensions due to increasing LT are still less pronounced compared to those caused by varying LED at the same LT. A transition from conduction to keyhole mode is observed when the energy input exceeds 0.60 J/mm which is consistent behavior across all LTs. With Mode 3, increasing the LT to 90 µm results in a modest but consistent increase in melt pool depth, accompanied by a more pronounced rise in height. However, greater variation and inconsistency are observed in melt pool width, suggesting an increasing difficulty in achieving uniform energy distribution with thicker layers, as also illustrated in Fig. 15 (c). The fluctuations in width indicate that as LT increases, maintaining uniform energy absorption and stable melting conditions becomes more challenging, leading to variations in melt pool geometry and potential process instabilities. In the case of Mode 6, significant fluctuations and instability in melt pool formation are observed with a 90 µm LT, particularly at lower LEDs (0.44–0.60 J/mm). Balling, lack of bonding, and protrusions become more pronounced (Supplementary Fig. S5 (c)), resulting in increased height and reduced width compared to melt pools formed with 30 µm and 60 µm layers at the same LED levels which ultimately impact the stability of the melt tracks, as illustrated in the stability map in Fig. 14(c). These effects suggest insufficient energy penetration and incomplete melting, resulting in surface irregularities

and weak interlayer bonding, as previously discussed in Section 3.1. However, as the laser energy input increases, the melt pool depth exhibits a slight increase, while the width expands, reaching a maximum of 413.22 μm at 1.0 J/mm, which surpasses the widths achieved with Mode 0 and Mode 3. Despite the increase in width, the melt pool height remains consistently high, indicating that energy absorption is limited by the thicker layer, leading to surface material accumulation rather than deep penetration or achieving the conduction mode, as also reported in previous studies [85,87].

The results further confirm the transition from conduction to keyholing, which is identified by the width-to-depth (W/D) ratio, as shown in Fig. 16. In this study, Transition-mode processing is observed when W/D $\leq$ 3, while complete keyholing occurs at W/D $\leq$ 2, marking the transition from a semi-circular conduction-mode melt pool to an elongated keyhole geometry. This threshold aligns with previous literature, where keyhole transitions occur at W/D values between 2 and 3 [62,88,89]. The results show that Mode 0 consistently produces lower W/D ratios (< 3), indicative of deeper melt pools and stronger keyholing tendencies. In contrast, Modes 3 and 6 exhibit higher W/D ratios (>5), producing wider, shallower melt pools that remain in conduction mode without transitioning to keyhole formation, regardless of LT. Additionally, the scattered data in Fig. 16(c) further highlights fluctuations due to increased LT. In addition to W/D, the H/D and H/W ratios offer further insight into melt pool geometry. A low H/D ratio typically indicates deep penetration with minimal vertical buildup, often associated with keyhole-mode melting. In contrast, higher H/D and H/W values suggest tall, narrow melt pools, which can be indicative of undermelting or insufficient fusion. These ratios are plotted in the Supplementary Information (Fig. S6), contributing additional perspective on melt pool morphology and stability, although these metrics are less commonly standardized in literature compared to W/D [90]. Furthermore, melt pool height is more susceptible to surface fluctuations, oxidation, powder droplet or re-solidified spatter on top surfaces, making H/D and H/W less consistent and more variable compared to depth and width measurements.

3.3.1. *Impact of melt pool dynamics on track stability*

The relationship between melt pool geometry and single-track stability is strongly influenced by LBS, LED, and LT, the primary variables examined in this study. The results demonstrate that variations in melt pool dimensions directly impact track continuity, defect formation, and overall part quality. The results indicate that melt pool dimensions, including width, depth, and height, play a critical role in determining the stability and continuity of single tracks which has an ultimate effect on the process productivity and overall quality of the parts. Insufficient laser energy input, combined with beam shape effects, destabilizes the melt pool, leading to surface defects such as balling, fragmentation, necking, and roughness. Mode 0 consistently produces deeper and narrower melt pools across all LTs. At lower energy inputs, the high energy concentration at the center of the beam leads to steep thermal gradients, resulting in narrow, continuous tracks. However, as energy density increases, excessive vaporization and recoil pressure drive spattering and keyhole formation, which introduces irregularities in track continuity and surface roughness. This confirms the direct impact of melt pool formation behavior on track formation and overall quality. Similar correlations between single-track formation and melt pool characteristics were observed in the study by Wischeropp et al. [36]. This explains why, in lower LT (30 μm), Mode 0 tracks maintain better continuity, whereas, with increased layer thickness (60–90 μm), uniform melting is compromised, leading to an increased prevalence of surface defects and balling due to inadequate fusion. Mode 3, with its more uniform energy distribution, produces balanced melt pool width and depth, resulting in relatively stable tracks at moderate energy inputs (0.55–0.80 J/mm). However, at lower LED (≤0.44 J/mm), protrusions in the melt pool correspond to the balling-up effect observed in tracks, caused by incomplete melting and localized solidification, as clearly observed in

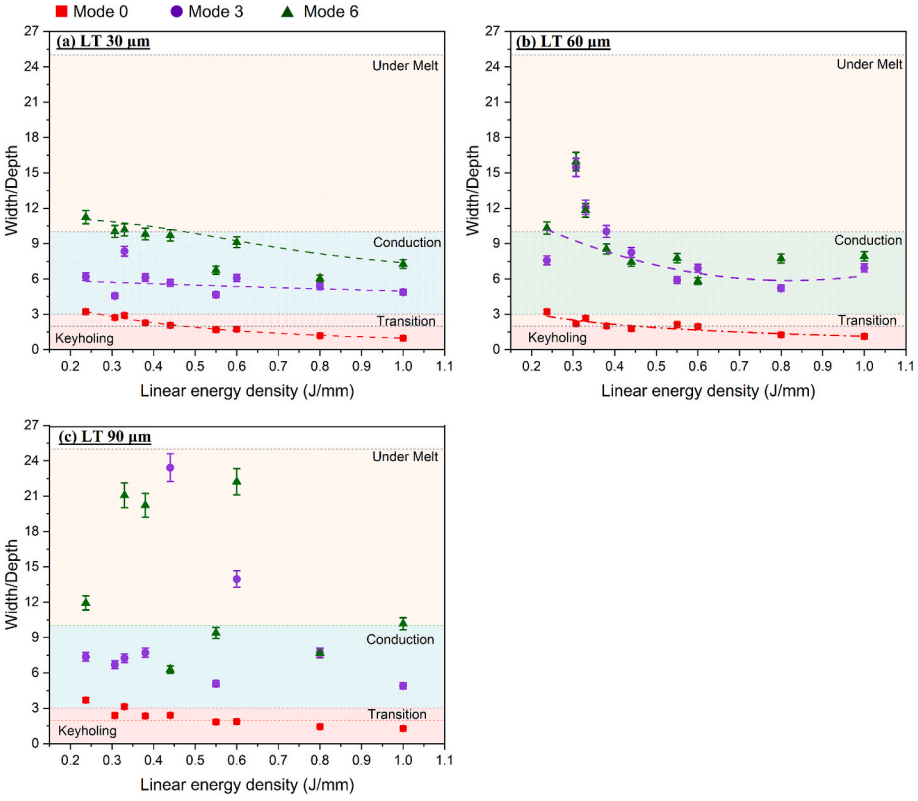

Fig. 16. Width-to-Depth (W/D) ratio of melt pools as a function of LED for three beam shapes, Mode 0, Mode 3, and Mode 6 at different layer thicknesses: (a) 30 μm, (b) 60 μm, and (c) 90 μm.

the reported results in section 3.1. Mode 6 forms the widest yet shallowest melt pools. It ensures stable and continuous tracks at higher energy inputs (≥0.8 J/mm) by promoting broader energy dispersion and improved surface coverage. The wider melt pools correlate with enhanced track stability and reduced balling tendencies. However, at lower LEDs, insufficient penetration leads to track discontinuities and powder adhesion. These findings align with studies indicating that beam shaping is crucial in controlling melt pool stability, with ring-shaped beams reducing sharp thermal gradients and improving track consistency [60,91].

3.4. Effect of areal energy density (J/mm^2)

Melt pool characteristics in PBF-LB/M are typically analyzed using linear energy density (E_l, J/mm), a key process control parameter. However, E_l does not fully capture the spatial energy distribution influenced by beam shaping. To better assess beam shape effects, the influence of areal energy density (E_a, J/mm^2) was also analyzed in this study, as it accounts for spot size and spatial energy distribution. Since different beam shapes alter spot size, their energy concentration varies, impacting pool width, penetration depth, and stability. While E_a provides insights into localized energy input, E_l still remains the primary metric due to its practical significance in PBF-LB/M process control, where power and scan speed are the primary adjustable parameters [92–94], and spot size is typically fixed. However, the variations in melt pool geometry at equivalent E_l values highlight the independent effect of beam shape, extending beyond energy density alone. This section expands on the previous discussion of beam-shaping effects by introducing E_a as an additional factor to further our understanding of melt pool formation. The analysis further clarifies how laser shaping interacts with the material response, complementing the previously discussed effects of E_l.

Fig. 17 illustrates the influence of E_a on melt pool width, depth, and height, highlighting significant variations across beam shapes and layer thicknesses and emphasizing the role of spatial energy distribution in melt pool formation. For LT = 30 μm (Fig. 17a), Mode 0 exhibits a gradual increase in melt pool width with increasing E_a, showing a nearly linear trend. Mode 3 follows a similar trend but maintains a consistently wider melt pool than Mode 0. Mode 6 produces the widest melt pools which are in the relatively lower $E_a$range as compared to Mode 0 and Mode 3. The melt pool depth increases for Mode 0, with a notable jump at 4.4 J/mm^2, demonstrating its higher energy concentration and stronger penetration capability, while Modes 3 and 6 maintain relatively shallow depths, supporting the conduction-mode melting behavior of ring-based beams. Melt pool height remains relatively low and stable across all modes, though Mode 6 exhibits slightly larger height fluctuations at lower E_a, indicating instabilities in track formation at reduced energy input. At LT = 60 μm (Fig. 17), the melt pool width trends remain consistent across all beam shapes, with Mode 6 maintaining the widest melt pools, followed by Mode 3, while Mode 0 remains the narrowest but deepest. However, compared to LT = 30 μm, melt pool width increases more rapidly at lower E_a due to increased energy absorption from the thicker layer. Mode 0 shows a significant rise in melt pool depth, reinforcing its strong keyholing tendency as E_a increases. Mode 3 and Mode 6 exhibit moderate increases in depth but remain in conduction mode. The melt pool height follows almost similar trend to LT = 30 μm but exhibits slightly greater variations, particularly in Mode 6 at lower in the lower E_a range, indicating increased instability due to thicker layers requiring higher energy input for uniform melting, as these similar trends were observed previously with various E_l. For LT =

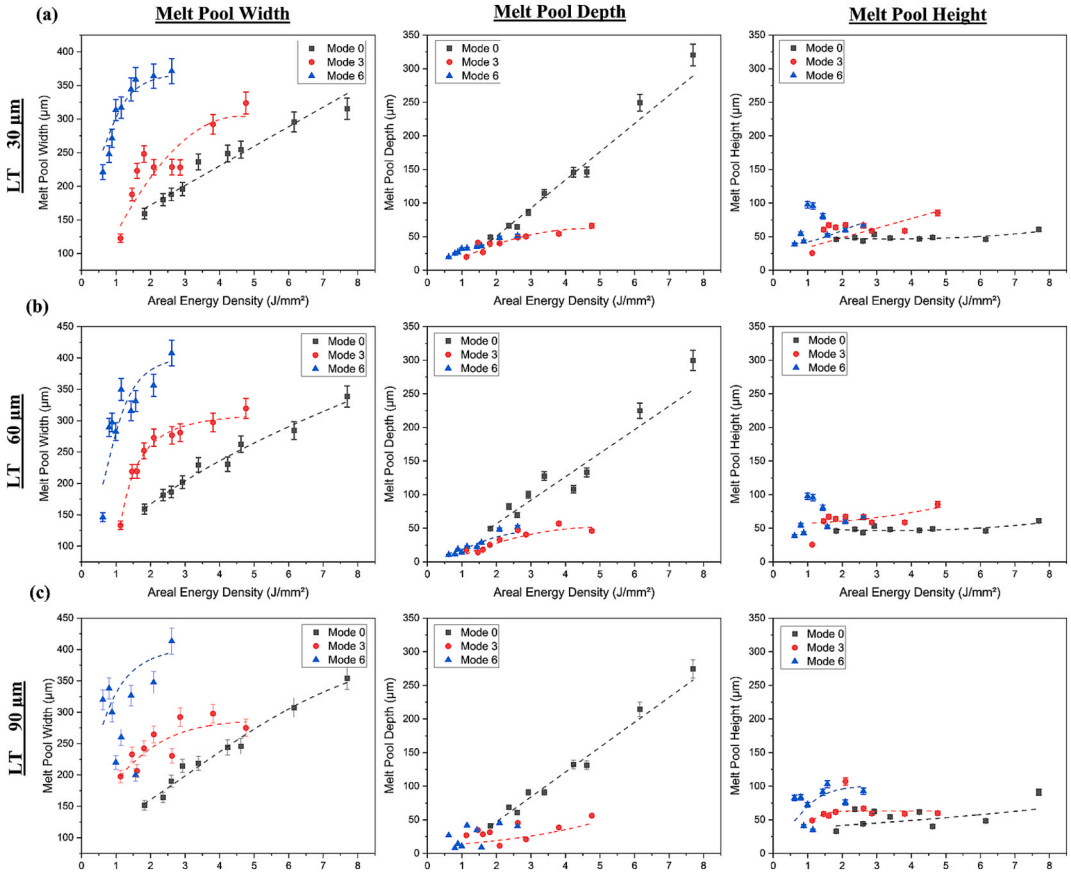

Fig. 17. Influence of Areal Energy Density (E_a) on melt pool width, depth, and height across different layer thicknesses (a) 30 μm, (b) 60 μm, and (c) 90 μm and for three beam modes: Mode 0, Mode 3, and Mode 6.

90 μm (Fig. 17c), melt pool width expands further across all modes, with Mode 6 continuing to produce the widest tracks due to its lateral energy spread but with notable fluctuations as most of the data points are not following the specific trend. However, the width increase is less pronounced compared to LT = 60 μm, indicating a saturation effect at higher LTs. Mode 0 shows a pronounced rise in melt pool depth, confirming its strong keyholing behavior at lower to higher E_a. Mode 3 and Mode 6 maintain relatively shallow depths, with Mode 6 displaying noticeable width-to-depth variations, which aligns with previous findings that ring beams mitigate keyholing but require sufficient energy input to avoid under-melting issues. Melt pool height is more variable in this case, particularly at lower E_a, where Mode 6 shows significant fluctuations, indicating increased instability in track formation at insufficient energy levels for thick layers.

The W/D ratio in Fig. 18 further highlights the effect of E_a on melting pool geometry across the three LTs. Mode 0 consistently exhibits the lowest W/D ratios, remaining below 3 across all LTs, confirming its strong penetration and keyholing tendency at higher E_a. In contrast, Mode 3 and Mode 6 produce significantly higher W/D ratios, particularly at lower E_a, where the melt pools are wider and shallower, remaining in conduction mode. As LT increases, the W/D ratio also increases, especially in Mode 6, where values exceed 24 at 90 μm, indicating extreme lateral spreading with minimal depth. The trend suggests that higher layer thickness amplifies the effect of beam shaping, leading to a greater difference between penetration-focused (Mode 0) and width-dominant (Mode 6) melt pools. At lower E_a. W/D fluctuations are more pronounced, particularly in Mode 3 and Mode 6, indicating instabilities in melt pool formation due to insufficient energy input for consistent depth formation.

3.5. Numerical analysis results

Numerical analysis was performed to elucidate the influence of beam shaping on melt pool formation in Ti-6Al-4V. The model was first calibrated against experimental data, as shown in Fig. 19, to ensure reliable predictions. The model predictions show good agreement with experimental measurements for all beam shapes, except for the keyhole regime observed in Mode 0. As shown in Table 3, the average error percentage between the experimentally measured and numerically predicted melt pool dimensions in Mode 0 is 4.04 % for the width and 3.76 % for the depth. These difference and error values fall within acceptable limits for thermal simulations and align with reported ranges in similar modelling studies [95]. Consequently, subsequent analyses focus on the conduction melting regime.

The numerical results indicate that the beam shape affects the melt pool shape where Mode 0 generates symmetric melt pools but Mode 3 and Mode 6 form nonsymmetric melt pools. Table 4 summarizes and presents a comparative overview of the melt pool characteristics including width, depth, and length and its geometry namely top view, cross-section view, and longitudinal view for Mode 0, Mode 3, and Mode 6 under a linear energy density of 0.38 J/mm. The results, corresponding to the top-view temperature distribution plots, reveal distinct differences in melt pool geometry and thermal profiles, which have direct implications for process stability and inter-layer bonding.

Mode 0, characterized by a concentrated central intensity, produces a symmetric melt pool with a width of 211 μm, a depth of 78 μm, and a length of 416 μm accompanied by a peak temperature at the center reaching 4603 K (see Fig. 20). The melt pool length (in the scanning direction) is long (416 μm), suggesting that the energy distribution remains effective over a larger area along the track. However, experimental observations indicate that, at higher linear energy densities, Mode 0 tends toward a keyhole-dominated process, which is undesirable in the PBF-LB/M process.

Mode 3, featuring an approximately equal split between the central Gaussian and the outer ring (β ≈ 0.44), produces a slightly wider melt pool (220 μm) with a shallower depth (60 μm) and a reduced melt pool length (306.5 μm) compared to Mode 0. The temperature distribution reveals a lower central peak (2790 K) and a more uniform profile due to

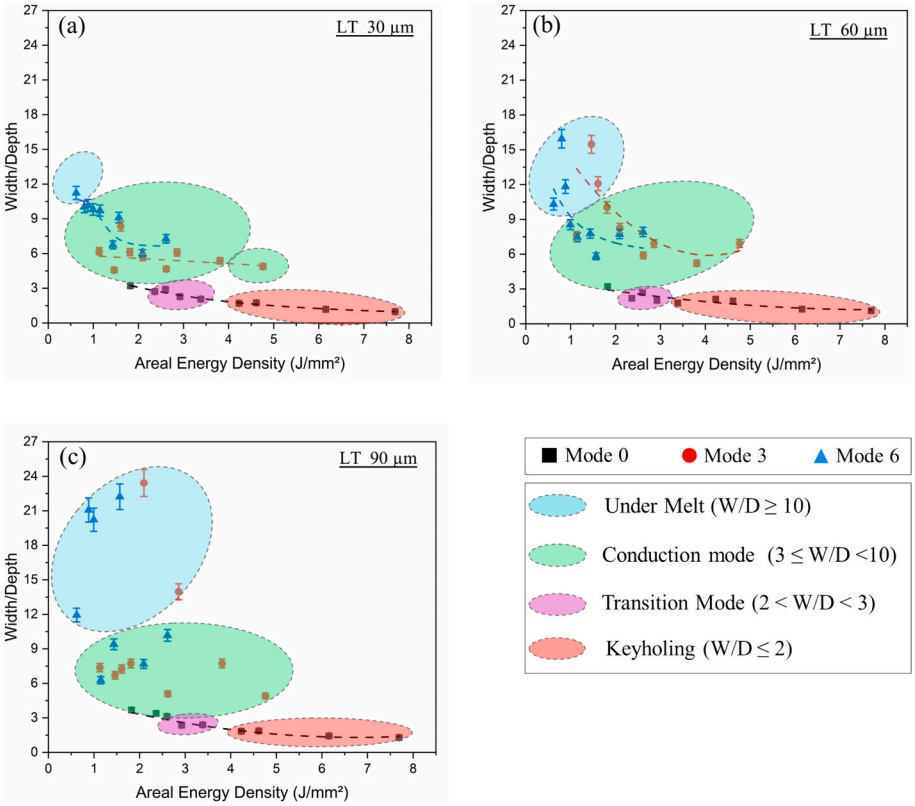

Fig. 18. Width-to-Depth (W/D) Ratio as a function of E_a for different layer thicknesses (30 μm, 60 μm, and 90 μm) and beam shapes (Mode 0, Mode 3, and Mode 6).

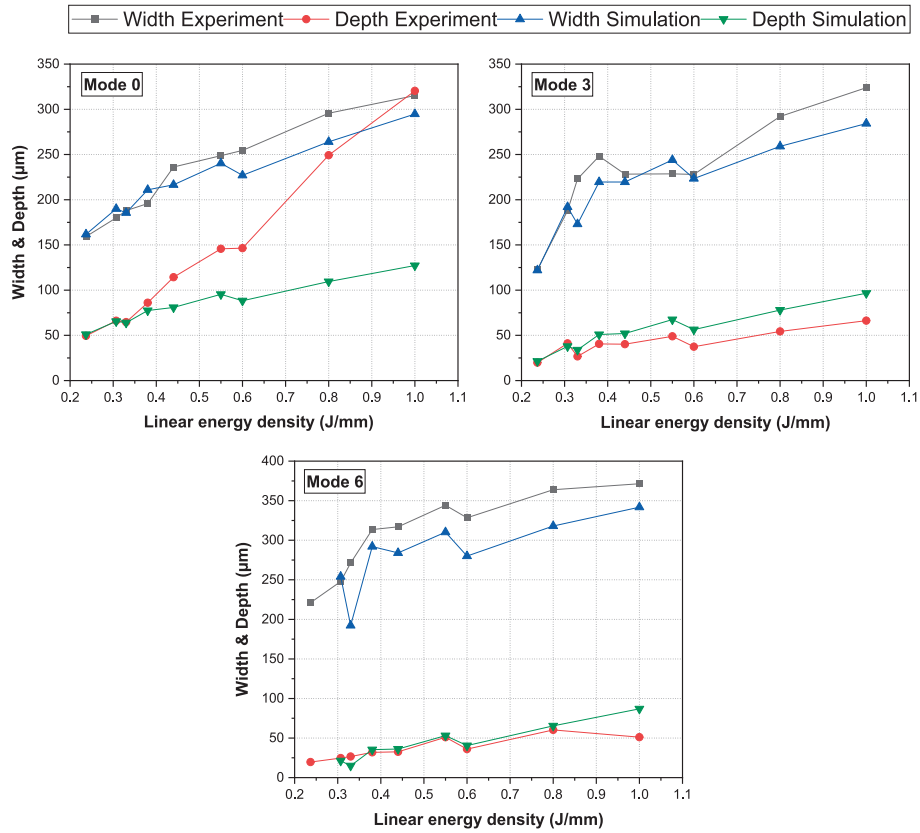

Fig. 19. Comparison between experimental and simulated melt pool width and depth for Mode 0, Mode 3, and Mode 6 considering a layer thickness of 30 μm.

Table 3
Error percentage between experimentally measured and numerically predicted melt pool dimensions for Mode 0.

	LED (J/mm)	Width Experiment (μm)	Width Simulation (μm)	Error %	Depth Experiment (μm)	Depth Simulation (μm)	Error %
Mode 0	0.237	159.24	161.76	1.58	49.44	51	3.15534
	0.307	180	190	5.56	66.149	65.5	0.981118
	0.33	188	185.6	1.28	64.64	64	0.990099
	0.38	195.81	211	7.76	86.04	77.5	9.925616
Average error %				4.043			3.76

preheating and post-heating effects from the outer ring. Notably, Mode 3 maintains a conduction melting regime even at higher linear energy densities, avoiding the transition to keyhole formation.

Mode 6, with a predominant ring intensity ($\beta \approx 0.1$, corresponding to ~ 90 % energy in the outer ring), generates the widest melt pool (292 μm) but the shallowest (35 μm) and shortest (253 μm) overall. The peak temperature is reduced to 2381 K, reflecting the distributed energy input. The higher intensity in the ring (~90 %) dominates the heat input to the powder layer, which produces a non-uniform melt pool similar to a half ring as shown in the top view plot. The higher intensity shift (~90 %) to the outer ring indicates that the energy in Mode 6 is distributed over a larger surface area, reducing the peak temperature and limiting the penetration depth. Although Mode 6 may facilitate larger melt footprints, it risks insufficient inter-layer fusion due to inadequate penetration.

Additionally, the thermal profiles in Fig. 20 illustrate the temperature distribution along the x-coordinate for the three beam profiles, providing insights into the impact of beam intensity distribution on the thermal behavior during the process. As the beam intensity shifts from a pure Gaussian (Mode 0) to a full ring (Mode 6), the peak temperature decreases, and the temperature field becomes more uniform. Mode 0 produces a high and sharply peaked temperature profile, indicative of a highly concentrated energy input. Although this can be beneficial for certain process conditions, it also increases the likelihood of keyhole formation at higher linear energy densities. By contrast, Mode 6 distributes most of the laser energy in the ring, lowering the peak temperature while widening the heated region. While broader energy distribution helps to maintain a more uniform thermal field and reduces the likelihood of localized overheating, it also results in a shallower melt pool. The reduced penetration may not provide the necessary bonding strength between layers, thereby compromising the mechanical integrity of the fabricated part. Mode 3, which splits the intensity between a central Gaussian core and a surrounding ring, exhibits intermediate behaviour. Its peak temperature is lower than that of Mode 0 yet remains sufficiently high to ensure stable conduction melting. Meanwhile, the ring component broadens the thermal gradient, thereby reducing sharp temperature drops and minimizing the risk of keyholing.

The developed model is calibrated for a specific layer thickness (i.e., 30 μm) used in this study. However, its applicability can be extended to other layer thicknesses with appropriate adjustments. The model accurately predicts melt pool dimensions for Mode 0 at increased layer thicknesses (e.g., 60 and 90 μm), but slight recalibration is necessary for Mode 3 and Mode 6 to maintain prediction accuracy. Nevertheless, the underlying physics implemented in the model remains valid, making it a robust framework for simulating a wide range of processing conditions, including variations in layer thickness.

Table 4
Melt pool top view, cross-section, and longitudinal section view for Mode 0, Mode 3, and Mode 6 under a linear energy density of $E_l = 0.38\ J/mm$ ($P = 250\ W$ and $V = 650\ mm/s$).

Mode 0

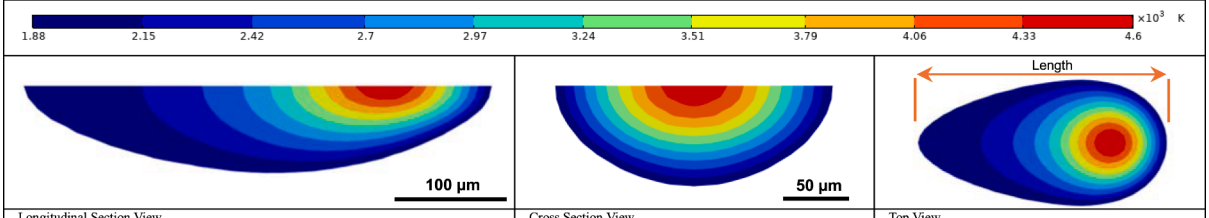

Longitudinal Section View | Cross Section View | Top View

Melt pool characteristics

Width	Depth	Length	Peak Temperature
211 µm	78 µm	416 µm	4603 K

Mode 3

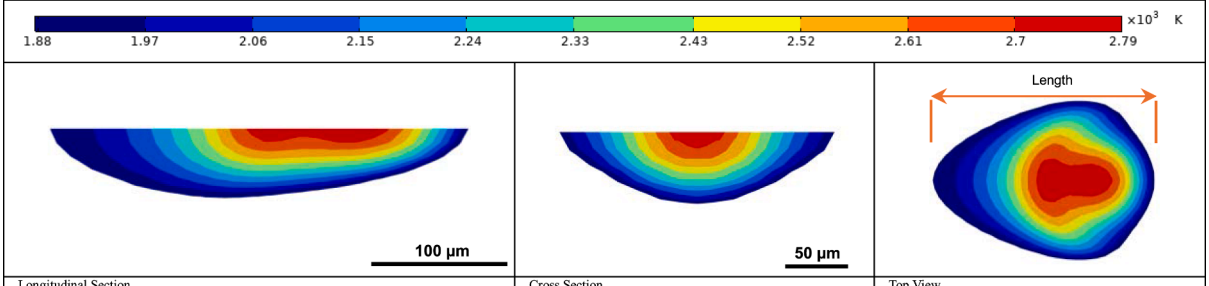

Longitudinal Section | Cross Section | Top View

Melt pool characteristics

Width	Depth	Length	Peak Temperature
220 µm	60 µm	306.5 µm	2790 K

Mode 6

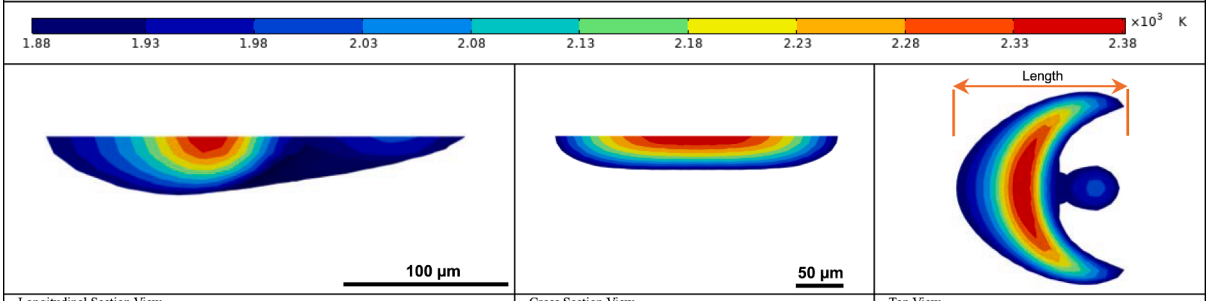

Longitudinal Section View | Cross Section View | Top View

Melt pool characteristics

Width	Depth	Length	Peak Temperature
292 µm	35 µm	253 µm	2381 K

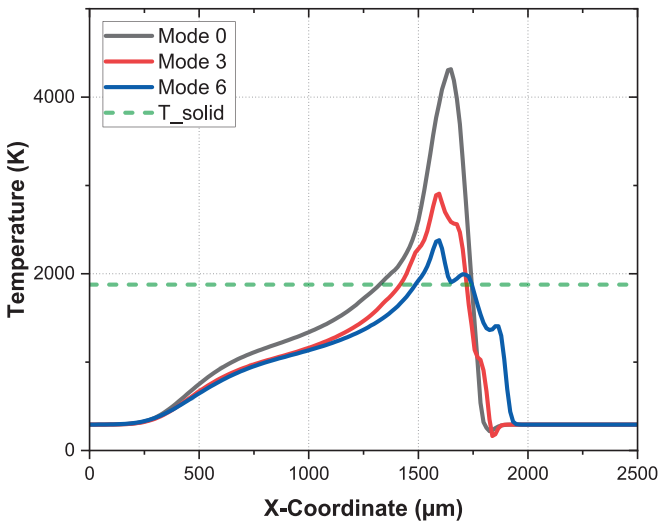

Fig. 20. Temperature profile plot for Mode 0, Mode 3, and Mode 6 along the x-coordinate under a linear energy density of $E_l = 0.38$ *J/mm* ($P = 250$ *W and* $V = 650$ *mm/s).*

In conclusion, the results illustrated in Fig. 20 and Table 4 confirm that a purely Gaussian beam (Mode 0) can induce keyhole formation at high energy densities, while a purely ring-shaped beam (Mode 6), despite providing improved lateral energy distribution and track stability, may offer limited penetration depth, which could affect inter-layer bonding in certain conditions. The hybrid configuration (Mode 3) offers a balanced approach, combining adequate penetration with broader thermal distribution to enhance process stability and inter-layer bonding [96].

4. Limitations and future outlook

The approach in this study provides fundamental insight into how beam shape, energy input, and layer thickness affect melt pool behavior and surface morphology, however, several aspects still remain open for future investigation. The specific influence of beam diameter variations, which may significantly alter energy absorption and melt pool geometry, was not fully decoupled in this work and should be addressed in future studies. Moreover, thermal accumulation was not directly measured, and future work could benefit from the integration of in-situ thermal monitoring techniques, such as infrared or multispectral thermal imaging, to better understand melt pool evolution and substrate heating. For more accurate predictive capability, future modeling efforts could benefit from advanced simulation techniques, such as space partitioning with dynamic 3D mesh adaptation [97] or computationally efficient multi-scale thermal modeling based on the enthalpy method [98], to better capture thermal behavior and melt pool evolution in complex PBF-LB/M scenarios.

To expand the process understanding beyond isolated tracks, further studies should investigate multi-layer and volumetric geometries, incorporating key process parameters like hatch spacing, scan strategy, and layer count. These studies would offer more realistic insight into how beam shaping affects inter-track bonding, porosity, and thermal history in practical builds. The approach could also be extended to lattice structures to explore how spatial energy distribution influences the manufacturability and performance of complex geometries. Finally, future work should aim to establish a more robust correlation between beam shape, resulting microstructure (e.g., grain morphology and phase content), and mechanical properties, which are critical for qualifying parts in high-performance applications [99,100].

5. Conclusion

This study investigates the effects of varying laser beam shapes in Aconity MIDI+ (Mode 0, Mode 3, Mode 6), layer thicknesses (30 μm, 60 μm, and 90 μm), and linear laser energy density (0.23 J/mm to 1.0 J/mm) on the single-tracks formation and stability, surface roughness and melt pool dynamics in the PBF-LB/M process of Ti-6Al-4V. The experimental findings and analysis provide valuable insights into parameter optimization to enhance track quality and process stability. Overall, this study demonstrated that the proper selection of beam shape, layer thickness, and energy input is vital for achieving uniform, and defect-free tracks, which are needed for the overall quality and efficiency of the PBF-LB/M process. The key findings of this study are included below:

1. Beam shape has a considerable impact on track width, stability, and surface quality, with ring-shaped beams (Mode 6) producing the widest and smoothest tracks, particularly at higher linear energy inputs. For instance, Mode 6 resulted in track widths up to 387.36 μm, showing a 22 % increase over Mode 0, while Mode 3 produced an average increase of 8.7 % in track width compared to Mode 0. The optimization of laser parameters and layer thickness for each beam profile is critical for improving melt pool size and shape, broadness of tracks, and reducing defects such as track segmentation, droplet ejection, partial fusion, and balling.
2. Surface roughness is highly dependent on beam profile and energy input. Beam shape Mode 0 generally results in lower roughness but shows more spattering and balling at higher linear energies, while Mode 3 and Mode 6 produce high roughness at lower energy inputs and improve at higher energy inputs, forming smoother single tracks due to more uniform energy distribution and reduced thermal gradients. Mode 6 achieved the lowest final roughness (~5.2 μm) at high LED, improving surface quality by over 30 % compared to Mode 0.
3. Beam shapes have a significant influence on melt pool size and dimensions. Mode 0 produced the deepest melt pools, reaching 325.4 μm in depth, but with narrower widths and W/D < 2, indicating keyhole tendency. Mode 3 showed balanced melt pools with depths around 146.5 μm and widths up to 313.5 μm, maintaining conduction mode. Mode 6 yielded the widest melt pools (up to 413.2 μm) but shallower depths, with W/D ratios exceeding 24, favoring lateral expansion and surface uniformity over penetration.
4. Thinner layers (~30 μm) are more suitable which produced stable and smoother tracks across all beam profiles, while thicker layers (≥60 μm) increased surface roughness and defects like spattering and balling, especially with Mode 0. The ring-shaped beam (Mode 6) leads to more stable track formation at higher energy inputs, particularly with thicker layers if the energy absorption is adequate. However, the depth of the melt pool is quite shallow even with high energy inputs while the height is raised which results in poor layer bonding.
5. The numerical analysis further confirmed that neither a fully Gaussian (Mode 0) nor a fully ring-shaped beam profile (Mode 6) is ideal for the PBF-LB/M process, particularly in applications where strong interlayer bonding and minimal defect formation are desired. In contrast, a hybrid core–ring beam profile is recommended to optimize melt pool characteristics by balancing a high central intensity with a broader peripheral distribution, thereby ensuring both sufficient penetration depth and uniform temperature distribution while mitigating keyholing. This recommendation is supported by both experimental and numerical results for layer thicknesses of 30–60 μm and linear energy densities in the range of 0.60–1.00 J/mm.
6. The incorporation of the areal energy density E_a analysis further emphasizes the role of beam shape and layer thickness in governing melt pool behavior. The findings confirm that Mode 0 promotes deeper penetration and keyholing tendencies, while Modes 3 and 6 prioritize lateral energy distribution, resulting in wider, shallower

melt pools that remain in conduction mode. Additionally, as layer thickness increases, the width-to-depth ratio (W/D) rises, particularly in Mode 6, leading to extreme lateral spreading (W/D > 24) but reduced depth stability at lower E_a.

7. The relationships between layer thickness, beam shape, and laser energy density are critical for achieving stable melt tracks and optimal melt pool stability. The numerical model validated these trends with an average error of 4.04 % in width and 3.76 % in depth for Mode 0, which aligns with accepted simulation accuracy standards.

CRediT authorship contribution statement

Abid Ullah: Writing – review & editing, Writing – original draft, Visualization, Validation, Software, Methodology, Investigation, Funding acquisition, Formal analysis, Data curation, Conceptualization. **Ahmad Reshad Bakhtari:** Software, Methodology, Writing – review & editing, Validation. **Alexander E. Medvedev:** Writing – review & editing, Visualization, Supervision, Resources, Formal analysis. **Andrey Molotnikov:** Writing – review & editing, Validation, Supervision, Project administration, Funding acquisition. **Dirk Herzog:** Writing – review & editing, Supervision, Resources. **Ingomar Kelbassa:** Writing – review & editing, Supervision, Project administration. **Claus Emmelmann:** Writing – review & editing, Supervision, Funding acquisition. **Milan Brandt:** Writing – review & editing, Validation, Supervision, Formal analysis, Conceptualization.

Declaration of competing interest

The authors declare that they have no known competing financial interests or personal relationships that could have appeared to influence the work reported in this paper.

Acknowledgments

This project has received funding from the European Union's Horizon 2020 Research and Innovation Program under the Marie Skłodowska-Curie Grant Agreement No. 101034328. This paper reflects only the author's view and the Research Executive Agency, and the European Commission are not responsible for any use that may be made of the information it contains. This work was supported by a fellowship of the German Academic Exchange Service (DAAD).

Appendix A. Supplementary data

Supplementary data to this article can be found online at https://doi.org/10.1016/j.optlastec.2025.113762.

Data availability

Supplementary materials are provided with this manuscript, and further data can be made available on request.

References

[1] J.M. Ravalji, S.J. Raval, Review of quality issues and mitigation strategies for metal powder bed fusion, Rapid Prototyp. J. 29 (2023) 792–817, https://doi.org/10.1108/RPJ-01-2022-0008.
[2] A. Das, A. Ghosh, S. Chattopadhyaya, C.-F. Ding, A review on critical challenges in additive manufacturing via laser-induced forward transfer, Opt. Laser Technol. 168 (2024) 109893, https://doi.org/10.1016/j.optlastec.2023.109893.
[3] L.P. Mocanu, C. Bellini, F. Berto, V. Di Cocco, F. Iacoviello, N. Razavi, 8 - Defects in additive manufacturing and their influence on structural integrity, in: Berto, F. and du Plessis, A. (eds.) Fatigue in Additive Manufactured Metals. pp. 181–21Elsevier (2024) Doi: 10.1016/B978-0-323-91204-4.00004-6.
[4] J. Bi, L. Wu, S. Li, Z. Yang, X. Jia, M.D. Starostenkov, G. Dong, Beam shaping technology and its application in metal laser additive manufacturing: a review, J. Mater. Res. Technol. 26 (2023) 4606–4628, https://doi.org/10.1016/j.jmrt.2023.08.037.
[5] T. Gutowski, S. Jiang, D. Cooper, G. Corman, M. Hausmann, J.-A. Manson, T. Schudeleit, K. Wegener, M. Sabelle, J. Ramos-Grez, D.P. Sekulic, Note on the rate and energy efficiency limits for additive manufacturing, J. Ind. Ecol. 21 (2017) S69–S79, https://doi.org/10.1111/jiec.12664.
[6] D. Gu, X. Shi, R. Poprawe, D.L. Bourell, R. Setchi, J. Zhu, Material-structure-performance integrated laser-metal additive manufacturing, Science (1979) 372, eabg1487 (2021). Doi: 10.1126/science.abg1487.
[7] A. Ullah, A. Ur Rehman, M.U. Salamci, F. Ptr, T. Liu, The influence of laser power and scanning speed on the microstructure and surface morphology of Cu2O parts in SLM, Rapid Prototyp. J. 28 (2022) 1796–1807, https://doi.org/10.1108/RPJ-12-2021-0342.
[8] A.U. Rehman, A. Ullah, T. Liu, R.U. Rehman, M.U. Salamci, Additive manufacturing of Al2O3 ceramics with MgO/SiC contents by laser powder bed fusion process, Front. Chem. 11 (2023), https://doi.org/10.3389/fchem.2023.1034473.
[9] H. Liu, D. Gu, L. Xi, H. Zhang, K. Shi, B. Wu, R. Zhang, J. Qi, High-performance aluminum-based materials processed by laser powder bed fusion: process, microstructure, defects and properties coordination, Additive Manuf. Front. 3 (2024) 200145, https://doi.org/10.1016/j.amf.2024.200145.
[10] S.M. Hosseini, E. Vaghefi, E. Mirkoohi, The role of defect structure and residual stress on fatigue failure mechanisms of Ti-6Al-4V manufactured via laser powder bed fusion: effect of process parameters and geometrical factors, J. Manuf. Process. 102 (2023) 549–563, https://doi.org/10.1016/j.jmapro.2023.07.014.
[11] A. Ullah, H. Wu, A. Ur Rehman, Y. Zhu, T. Liu, K. Zhang, Influence of laser parameters and Ti content on the surface morphology of L-PBF fabricated Titania, Rapid Prototyp. J. 27 (2021) 71–80, https://doi.org/10.1108/RPJ-03-2020-0050.
[12] P. Kahhal, Y.-K. Jo, S.-H. Park, Recent progress in remanufacturing technologies using metal additive manufacturing processes and surface treatment, Int. J. Precision Eng. Manuf.-Green Technol. 11 (2024) 625–658, https://doi.org/10.1007/s40684-023-00551-2.
[13] Z. Yan, W. Liu, Z. Tang, X. Liu, N. Zhang, M. Li, H. Zhang, Review on thermal analysis in laser-based additive manufacturing, Opt. Laser Technol. 106 (2018) 427–441, https://doi.org/10.1016/j.optlastec.2018.04.034.
[14] N.C. Levkulich, S.L. Semiatin, J.E. Gockel, J.R. Middendorf, A.T. DeWald, N. W. Klingbeil, The effect of process parameters on residual stress evolution and distortion in the laser powder bed fusion of Ti-6Al-4V, Addit. Manuf. 28 (2019) 475–484, https://doi.org/10.1016/j.addma.2019.05.015.
[15] J. Elambasseril, J. Rogers, C. Wallbrink, D. Munk, M. Leary, M. Qian, Laser powder bed fusion additive manufacturing (LPBF-AM): the influence of design features and LPBF variables on surface topography and effect on fatigue properties, Crit. Rev. Solid State Mater. Sci. 48 (2023) 132–168, https://doi.org/10.1080/10408436.2022.2041396.
[16] D. Simson, S.K. Subbu, Effect of process parameters on surface integrity of LPBF Ti6Al4V, Procedia CIRP 108 (2022) 716–721, https://doi.org/10.1016/j.procir.2022.03.111.
[17] A. Ullah, M. Shah, Z. Ali, K. Asami, A. Ur Rehman, C. Emmelmann, Additive manufacturing of ceramics via the laser powder bed fusion process, Int. J. Appl. Ceram. Technol. 22 (2025) e15087, https://doi.org/10.1111/ijac.15087.
[18] F.M. Dickey, F.M. Dickey, T.E. Lizotte, S.C. Holswade, D.L. Shealy, (Eds.), Laser Beam Shaping Applications (1st ed.), CRC Press, , 2006.
[19] F. Asadi, A. Olleak, J. Yi, Y. Guo, Gaussian Process (GP)-based Learning Control of Selective Laser Melting Process, 2021, doi: 10.48550/arXiv.2010.04712.
[20] F. Galbusera, L. Caprio, B. Previtali, A.G. Demir, The influence of novel beam shapes on melt pool shape and mechanical properties of LPBF produced Al-alloy, J. Manuf. Process. 85 (2023) 1024–1036, https://doi.org/10.1016/j.jmapro.2022.12.007.
[21] C. Galy, E. Le Guen, E. Lacoste, C. Arvieu, Main defects observed in aluminum alloy parts produced by SLM: from causes to consequences, Addit. Manuf. 22 (2018) 165–175, https://doi.org/10.1016/j.addma.2018.05.005.
[22] A. Ur Rehman, M.A. Mahmood, P. Ansari, F. Pitir, M.U. Salamci, A.C. Popescu, I. N. Mihailescu, Spatter formation and splashing induced defects in laser-based powder bed fusion of AlSi10Mg Alloy: a novel hydrodynamics modelling with empirical testing, Metals (Basel) 11 (2021), https://doi.org/10.3390/met11122023.
[23] S. Sanchez, A. Zafari, L. Caprio, A.G. Demir, D. Jafari, Temporal and spatial beam shaping in LPBF for fine and porous Ti-alloy structures for regenerative fuel cell applications, Lasers Manuf. Mater. Process. 11 (2024) 154–178, https://doi.org/10.1007/s40516-023-00244-3.
[24] J.D. Pérez-Ruiz, F. Galbusera, L. Caprio, B. Previtali, L.N.L. de Lacalle, A. Lamikiz, A.G. Demir, Laser beam shaping facilitates tailoring the mechanical properties of IN718 during powder bed fusion, J. Mater. Process. Technol. 328 (2024) 118393, https://doi.org/10.1016/j.jmatprotec.2024.118393.
[25] G.Y. Belay, Y. Kinds, L. Goossens, K. Gurung, N. Bosmans, R. Diltoer, J. Eraly, M. Vervaeke, H. Thienpont, B. Van Hooreweder, J. Van Erps, Dynamic optical beam shaping system to generate Gaussian and top-hat laser beams of various sizes with circular and square footprint for Additive Manufacturing applications, Procedia CIRP 111 (2022) 75–80, https://doi.org/10.1016/j.procir.2022.08.134.
[26] A.R. Bakhtari, H.K. Sezer, O.E. Canyurt, O. Eren, M. Shah, S. Marimuthu, A review on laser beam shaping application in laser-powder bed fusion, Adv. Eng. Mater. 26 (2024) 2302013, https://doi.org/10.1002/adem.202302013.
[27] J. Bi, L. Wu, S. Li, Z. Yang, X. Jia, M.D. Starostenkov, G. Dong, Beam shaping technology and its application in metal laser additive manufacturing: a review, J. Mater. Res. Technol. 26 (2023) 4606–4628, https://doi.org/10.1016/j.jmrt.2023.08.037.

[28] M. Mehrpouya, A. Gisario, M. Elahinia, Laser welding of NiTi shape memory alloy: a review, J. Manuf. Process. 31 (2018) 162–186, https://doi.org/10.1016/j.jmapro.2017.11.011.

[29] A.L. Rominiyi, P.M. Mashinini, A critical review of microstructure and mechanical properties of laser welded similar and dissimilar titanium alloy joints, J. Adv. Joining Processes 9 (2024) 100191, https://doi.org/10.1016/j.jajp.2024.100191.

[30] K.Y. Benyounis, A.G. Olabi, M.S.J. Hashmi, Effect of laser welding parameters on the heat input and weld-bead profile, J. Mater. Process. Technol. 164–165 (2005) 978–985, https://doi.org/10.1016/j.jmatprotec.2005.02.060.

[31] D.L. Shealy, J.A. Hoffnagle, Laser beam shaping profiles and propagation, Appl. Opt. 45 (2006) 5118–5131, https://doi.org/10.1364/AO.45.005118.

[32] Y. Mi, S. Mahade, F. Sikström, I. Choquet, S. Joshi, A. Ancona, Conduction mode laser welding with beam shaping using a deformable mirror, Opt. Laser Technol. 148 (2022) 107718, https://doi.org/10.1016/j.optlastec.2021.107718.

[33] S. Liu, G. Mi, F. Yan, C. Wang, P. Jiang, Correlation of high power laser welding parameters with real weld geometry and microstructure, Opt. Laser Technol. 94 (2017) 59–67, https://doi.org/10.1016/j.optlastec.2017.03.004.

[34] C. Kumar, M. Das, C.P. Paul, K.S. Bindra, Comparison of bead shape, microstructure and mechanical properties of fiber laser beam welding of 2 mm thick plates of Ti-6Al-4V alloy, Opt. Laser Technol. 105 (2018) 306–321, https://doi.org/10.1016/j.optlastec.2018.02.021.

[35] P. Zhang, Z. Jia, Z. Yu, H. Shi, S. Li, D. Wu, H. Yan, X. Ye, J. Chen, F. Wang, Y. Tian, A review on the effect of laser pulse shaping on the microstructure and hot cracking behavior in the welding of alloys, Opt. Laser Technol. 140 (2021) 107094, https://doi.org/10.1016/j.optlastec.2021.107094.

[36] T. Wischeropp, Advancement of Selective Laser Melting by Laser Beam Shaping, 2021, Doi: 10.1007/978-3-662-64585-7.

[37] L.E. Loh, Z.H. Liu, D.Q. Zhang, M. Mapar, S.L. Sing, C.K. Chua, W.Y. Yeong, Selective Laser Melting of aluminium alloy using a uniform beam profile, Virtual Phys Prototyp. 9 (2014) 11–16, https://doi.org/10.1080/17452759.2013.869608.

[38] M.C. Sow, T. De Terris, O. Castelnau, Z. Hamouche, F. Coste, R. Fabbro, P. Peyre, Influence of beam diameter on Laser Powder Bed Fusion (L-PBF) process, Addit. Manuf. 36 (2020) 101532, https://doi.org/10.1016/j.addma.2020.101532.

[39] C. Tenbrock, F.G. Fischer, K. Wissenbach, J.H. Schleifenbaum, P. Wagenblast, W. Meiners, J. Wagner, Influence of keyhole and conduction mode melting for top-hat shaped beam profiles in laser powder bed fusion, J. Mater. Process. Technol. 278 (2020) 116514, https://doi.org/10.1016/j.jmatprotec.2019.116514.

[40] A. Okunkova, M. Volosova, P. Peretyagin, Y. Vladimirov, I. Zhirnov, A. V. Gusarov, Experimental approbation of selective laser melting of powders by the use of non-gaussian power density distributions, Phys. Procedia 56 (2014) 48–57, https://doi.org/10.1016/j.phpro.2014.08.095.

[41] A.A. Okunkova, P.Y. Peretyagin, P.A. Podrabinnik, I.V. Zhirnov, A.V. Gusarov, Development of laser beam modulation assets for the process productivity improvement of selective laser melting, Procedia IUTAM 23 (2017) 177–186, https://doi.org/10.1016/j.piutam.2017.06.019.

[42] Z. Liu, B. He, T. Lyu, Y. Zou, A review on additive manufacturing of titanium alloys for aerospace applications: directed energy deposition and beyond Ti-6Al-4V, JOM 73 (2021) 1804–1818, https://doi.org/10.1007/s11837-021-04670-6.

[43] M.R. Bandekhoda, M.H. Mosallanejad, M. Atapour, L. Iuliano, A. Saboori, Investigation on the potential of laser and electron beam additively manufactured Ti–6Al–4V components for orthopedic applications, Met. Mater. Int. 30 (2024) 114–126, https://doi.org/10.1007/s12540-023-01496-6.

[44] C.B. Carolo, L. Cooper O, R.E., A review on the influence of process variables on the surface roughness of Ti-6Al-4V by electron beam powder bed fusion, Addit. Manuf. 59 (2022) 103103, https://doi.org/10.1016/j.addma.2022.103103.

[45] M.A. Buhairi, F.M. Foudzi, F.I. Jamhari, A.B. Sulong, N.A.M. Radzuan, N. Muhamad, I.F. Mohamed, A.H. Azman, W.S.W. Harun, M.S.H. Al-Furjan, Review on volumetric energy density: influence on morphology and mechanical properties of Ti6Al4V manufactured via laser powder bed fusion, Prog. Addit. Manuf. 8 (2023) 265–283, https://doi.org/10.1007/s40964-022-00328-0.

[46] T. Stoll, R. Prudlik, M. Birg, K. Wudy, Influence of different beam shapes on melt pool geometry of single melt tracks on IN718, Prog. Addit. Manuf. (2024), https://doi.org/10.1007/s40964-024-00775-x.

[47] J. Grünewald, V. Blickle, M. Allenberg-Rabe, P. Wagenblast, K. Wudy, Flexible and highly dynamic beam shaping for laser-based powder bed fusion of metals, Procedia CIRP 111 (2022) 65–70, https://doi.org/10.1016/j.procir.2022.08.124.

[48] P. Stavropoulos, H. Bikas, K. Tzimanis, N. Porevopoulos, A.N. Pilagatti, E. Atzeni, L. Iuliano, A. Salmi, Process window development of DED-LB/M process with coaxial wire for stainless steel AISI 316L, Int. J. Exp. Des. Process Optim. 7 (2024) 1–26, https://doi.org/10.1504/IJEDPO.2024.138131.

[49] A. Neira-Arce, Thermal modeling and simulation of electron beam melting for rapid prototyping on Ti6Al4V alloys, 2012, https://repository.lib.ncsu.edu/items/ef68b3f5-1653-4266-800b-d14836c80829.

[50] C.H. Fu, Y.B. Guo, Three-dimensional temperature gradient mechanism in selective laser melting of Ti-6Al-4V, J. Manuf. Sci. Eng. 136 (2014), https://doi.org/10.1115/1.4028539.

[51] S. Liu, H. Zhu, G. Peng, J. Yin, X. Zeng, Microstructure prediction of selective laser melting AlSi10Mg using finite element analysis, Mater. Des. 142 (2018) 319–328, https://doi.org/10.1016/j.matdes.2018.01.022.

[52] L. Vanmunster, L. Goossens, Y. Kinds, B. Van Hooreweder, B. Vrancken, Effect of a variable laser beam profile system on productivity and surface quality of 316L stainless steel parts produced by Laser Powder Bed Fusion, CIRP Ann. (2023), https://doi.org/10.1016/j.cirp.2023.04.035.

[53] N. Bannach, Phase Change: Cooling and Solidification of Metal, https://www.comsol.com/blogs/phase-change-cooling-solidification-metal/.

[54] W. Di, Y. Yongqiang, S. Xubin, C. Yonghua, Study on energy input and its influences on single-track,multi-track, and multi-layer in SLM, Int. J. Adv. Manuf. Technol. 58 (2012) 1189–1199, https://doi.org/10.1007/s00170-011-3443-y.

[55] D. Simson, C.P. Paul, S.K. Subbu, Experimental study and neural network model based prediction of layer thickness influence on LPBF IN625 single track geometry, Opt. Laser Technol. 173 (2024) 110543, https://doi.org/10.1016/j.optlastec.2024.110543.

[56] C. Guo, Z. Xu, Y. Zhou, S. Shi, G. Li, H. Lu, Q. Zhu, R.M. Ward, Single-track investigation of IN738LC superalloy fabricated by laser powder bed fusion: Track morphology, bead characteristics and part quality, J. Mater. Process. Technol. 290 (2021) 117000, https://doi.org/10.1016/j.jmatprotec.2020.117000.

[57] C. Guo, Z. Xu, Y. Zhou, S. Shi, G. Li, H. Lu, Q. Zhu, R.M. Ward, Single-track investigation of IN738LC superalloy fabricated by laser powder bed fusion: Track morphology, bead characteristics and part quality, J. Mater. Process. Technol. 290 (2021) 117000, https://doi.org/10.1016/j.jmatprotec.2020.117000.

[58] J. Chen, Y. Yang, Y. Bai, D. Wang, C. Zhao, J. Ying Hsi Fuh, Single and multiple track formation mechanism of laser powder bed fusion 316L/CuSn10 multi-material, Mater. Charact. 183 (2022) 111654, https://doi.org/10.1016/j.matchar.2021.111654.

[59] J. Chen, Y. Yang, Y. Bai, D. Wang, C. Zhao, J. Ying Hsi Fuh, Single and multiple track formation mechanism of laser powder bed fusion 316L/CuSn10 multi-material, Mater. Charact. 183 (2022) 111654, https://doi.org/10.1016/j.matchar.2021.111654.

[60] A. Ebrahimi, M. Sattari, A. Babu, A. Sood, G.-W. Römer, M. Hermans, Revealing the effects of laser beam shaping on melt pool behaviour in conduction-mode laser melting, J. Mater. Res. Technol. 27 (2023) 3955–3967, https://doi.org/10.1016/j.jmrt.2023.11.046.

[61] C. Zöller, N.A. Adams, S. Adami, Beam-shaping in laser-based powder bed fusion of metals: a computational analysis of point-ring intensity profiles, Addit. Manuf. 93 (2024) 104402, https://doi.org/10.1016/j.addma.2024.104402.

[62] T.M. Wischeropp, H. Tarhini, C. Emmelmann, Influence of laser beam profile on the selective laser melting process of AlSi10Mg, J. Laser Appl. 32 (2020), https://doi.org/10.2351/7.0000100.

[63] T. Zhang, H. Li, S. Liu, S. Shen, H. Xie, W. Shi, G. Zhang, B. Shen, L. Chen, B. Xiao, M. Wei, Evolution of molten pool during selective laser melting of Ti–6Al–4V, J. Phys. D Appl. Phys. 52 (2019) 055302, https://doi.org/10.1088/1361-6463/aaee04.

[64] S.A. Khairallah, A. Anderson, Mesoscopic simulation model of selective laser melting of stainless steel powder, J. Mater. Process. Technol. 214 (2014) 2627–2636, https://doi.org/10.1016/j.jmatprotec.2014.06.001.

[65] M. Brandt, Laser Additive Manufacturing- Materials, Design, Technologies and Applications, 2016.

[66] J. Wang, R. Zhu, Y. Liu, L. Zhang, Understanding melt pool characteristics in laser powder bed fusion: an overview of single- and multi-track melt pools for process optimization, Adv. Powder Mater. 2 (2023) 100137, https://doi.org/10.1016/j.apmate.2023.100137.

[67] S. Chowdhury, N. Yadaiah, C. Prakash, S. Ramakrishna, S. Dixit, L.R. Gupta, D. Buddhi, Laser powder bed fusion: a state-of-the-art review of the technology, materials, properties & defects, and numerical modelling, J. Mater. Res. Technol. 20 (2022) 2109–2172, https://doi.org/10.1016/j.jmrt.2022.07.121.

[68] T.T. Roehling, R. Shi, S.A. Khairallah, J.D. Roehling, G.M. Guss, J.T. McKeown, M.J. Matthews, Controlling grain nucleation and morphology by laser beam shaping in metal additive manufacturing, Mater. Des. 195 (2020) 109071, https://doi.org/10.1016/j.matdes.2020.109071.

[69] A.N. Soe, A. Sombatmai, P. Promoppatum, V. Srimaneepong, V. Trachoo, P. Pandee, Effect of post-processing treatments on surface roughness and mechanical properties of laser powder bed fusion of Ti–6Al–4V, J. Mater. Res. Technol. 32 (2024) 3788–3803, https://doi.org/10.1016/j.jmrt.2024.08.197.

[70] T.T. Opoz, A. Burgess, J.I. Ahuir-Torres, H.R. Kotadia, S. Tammas-Williams, The effect of surface finish and post-processing on mechanical properties of 17-4 PH stainless steel produced by the atomic diffusion additive manufacturing process (ADAM), Int. J. Adv. Manuf. Technol. 130 (2024) 4053–4066, https://doi.org/10.1007/s00170-024-12949-6.

[71] L. Cao, J. Li, J. Hu, H. Liu, Y. Wu, Q. Zhou, Optimization of surface roughness and dimensional accuracy in LPBF additive manufacturing, Opt. Laser Technol. 142 (2021) 107246, https://doi.org/10.1016/j.optlastec.2021.107246.

[72] A. Bhatt, Y. Huang, C.L.A. Leung, G. Soundarapandiyan, S. Marussi, S. Shah, R. C. Atwood, M.E. Fitzpatrick, M.K. Tiwari, P.D. Lee, In situ characterisation of surface roughness and its amplification during multilayer single-track laser powder bed fusion additive manufacturing, Addit. Manuf. 77 (2023) 103809, https://doi.org/10.1016/j.addma.2023.103809.

[73] F. Nahr, D. Bartels, R. Rothfelder, M. Schmidt, Influence of novel beam shapes on laser-based processing of high-strength aluminium alloys on the basis of EN AW-5083 single weld tracks, J. Manuf. Mater. Process. 7 (2023), https://doi.org/10.3390/jmmp7030093.

[74] N.T. Aboulkhair, I. Maskery, C. Tuck, I. Ashcroft, N.M. Everitt, On the formation of AlSi10Mg single tracks and layers in selective laser melting: Microstructure and nano-mechanical properties, J. Mater. Process. Technol. 230 (2016) 88–98, https://doi.org/10.1016/j.jmatprotec.2015.11.016.

[75] S. Brudler, A.E. Medvedev, C. Pandelidi, S. Piegert, T. Illston, M. Qian, M. Brandt, Systematic investigation of performance and productivity in laser powder bed fusion of Ti6Al4V up to 300 μm layer thickness, J. Mater. Process. Technol. 330 (2024) 118450, https://doi.org/10.1016/j.jmatprotec.2024.118450.

[76] J. Berez, C. Saldaña, On the nature and causes of spatter redistribution in laser powder bed fusion, J. Manuf. Process. 127 (2024) 531–544, https://doi.org/10.1016/j.jmapro.2024.07.143.
[77] Z. Ren, G. Fu, F. Liu, S. Mao, R. Gao, J. Jiang, Z. Tang, Elucidation of laser irradiation behaviors associated with the keyhole dynamics during laser powder bed fusion, J. Mater. Res. Technol. 32 (2024) 1672–1682, https://doi.org/10.1016/j.jmrt.2024.08.019.
[78] Y. Wang, W. Guo, Y. Xie, H. Li, C. Zeng, M. Xu, H. Zhang, In-situ monitoring plume, spattering behavior and revealing their relationship with melt flow in laser powder bed fusion of nickel-based superalloy, J. Mater. Sci. Technol. 177 (2024) 44–58, https://doi.org/10.1016/j.jmst.2023.07.068.
[79] E. Correa-Gómez, H. Castro-Espinosa, A. Caballero-Ruiz, E. García-López, L. Ruiz-Huerta, Effect of process parameters on the roughness and tensile behavior of parts manufactured by the metals LPBF process, Eng. Rep. n/a (2024) e12904, https://doi.org/10.1002/eng2.12904.
[80] D.S. Subbu, Effect of process parameters on surface integrity of LPBF Ti6Al4V, Procedia CIRP 108 (2022) 716–721, https://doi.org/10.1016/j.procir.2022.03.111.
[81] K. Mumtaz, N. Hopkinson, Top surface and side roughness of Inconel 625 parts processed using selective laser melting, Rapid Prototyp. J. 15 (2009) 96–103, https://doi.org/10.1108/13552540910943397.
[82] J. Ramos, D. Bourell, J. Beaman, Surface over-melt during laser polishing of indirect-SLS metal parts, MRS Proc. 758 (2002), https://doi.org/10.1557/PROC-758-LL1.9.
[83] H. Chen, D. Gu, J. Xiong, M. Xia, Improving additive manufacturing processability of hard-to-process overhanging structure by selective laser melting, J. Mater. Process. Technol. 250 (2017) 99–108, https://doi.org/10.1016/j.jmatprotec.2017.06.044.
[84] R. Cunningham, C. Zhao, N. Parab, C. Kantzos, J. Pauza, K. Fezzaa, T. Sun, A. D. Rollett, Keyhole threshold and morphology in laser melting revealed by ultrahigh-speed x-ray imaging, Science 1979 (363) (2019) 849–852, https://doi.org/10.1126/science.aav4687.
[85] F. Galbusera, L. Caprio, B. Previtali, A.G. Demir, The influence of novel beam shapes on melt pool shape and mechanical properties of LPBF produced Al-alloy, J. Manuf. Process. 85 (2023) 1024–1036, https://doi.org/10.1016/j.jmapro.2022.12.007.
[86] M. Bayat, R. Rothfelder, K. Schwarzkopf, A. Zinoviev, O. Zinovieva, C. Spurk, M. Hummel, A. Olowinsky, F. Beckmann, J. Moosmann, M. Schmidt, J.H. Hattel, Exploring spatial beam shaping in laser powder bed fusion: High-fidelity simulation and in-situ monitoring, Addit. Manuf. 104420 (2024), https://doi.org/10.1016/j.addma.2024.104420.
[87] I. Rosenthal, J.S. Weaver, S. Moylan, The influence of the melt pool structure on the mechanical properties of laser powder bed fusion Nickel Superalloy 625, Mater. Today Commun. 36 (2023) 106810, https://doi.org/10.1016/j.mtcomm.2023.106810.
[88] C. Zhao, K. Fezzaa, R.W. Cunningham, H. Wen, F. De Carlo, L. Chen, A.D. Rollett, T. Sun, Real-time monitoring of laser powder bed fusion process using high-speed X-ray imaging and diffraction, Sci. Rep. 7 (2017) 3602, https://doi.org/10.1038/s41598-017-03761-2.
[89] F.O. Olsen, Hybrid laser-arc welding, Woodhead Pub.; CRC Press (2009).
[90] M. Letenneur, A. Kreitcberg, V. Brailovski, Optimization of laser powder bed fusion processing using a combination of melt pool modeling and design of experiment approaches: Density control, J. Manuf. Mater. Process. 3 (2019), https://doi.org/10.3390/jmmp3010021.
[91] J. Grünewald, F. Gehringer, M. Schmöller, K. Wudy, Influence of ring-shaped beam profiles on process stability and productivity in laser-based powder bed fusion of AISI 316L, Metals (Basel) 11 (2021), https://doi.org/10.3390/met11121989.
[92] T. Yang, T. Liu, W. Liao, E. MacDonald, H. Wei, C. Zhang, X. Chen, K. Zhang, Laser powder bed fusion of AlSi10Mg: Influence of energy intensities on spatter and porosity evolution, microstructure and mechanical properties, J. Alloys Compd. 849 (2020) 156300, https://doi.org/10.1016/j.jallcom.2020.156300.
[93] P. Manikandan, K. Venkatesan, The influence of linear energy density on density, defect formation, residual stress, microstructure, and texture in 310 austenitic stainless steel by laser powder bed fusion, J. Manuf. Process. 131 (2024) 2191–2207, https://doi.org/10.1016/j.jmapro.2024.10.022.
[94] R. Zhao, A. Shmatok, R.D. Fischer, B.C. Prorok, Linking alloy thermo-physical behavior to laser process parameters for density optimization in LPBF, Int. J. Adv. Manuf. Technol. 129 (2023) 3171–3183, https://doi.org/10.1007/s00170-023-12501-y.
[95] P. Stavropoulos, G. Pastras, K. Tzimanis, N. Bourlesas, Addressing the challenge of process stability control in wire DED-LB/M process, CIRP Ann. 73 (2024) 129–132, https://doi.org/10.1016/j.cirp.2024.04.021.
[96] H.E. Sabzi, P.E.J. Rivera-Díaz-del-Castillo, Defect prevention in selective laser melting components: compositional and process effects, Materials 12 (2019) 3791, https://doi.org/10.3390/ma12223791.
[97] P. Foteinopoulos, A. Papacharalampopoulos, P. Stavropoulos, Additive manufacturing simulations: an approach based on space partitioning and dynamic 3D mesh adaptation, Addit. Manuf. Lett. 11 (2024) 100256, https://doi.org/10.1016/j.addlet.2024.100256.
[98] P. Stavropoulos, G. Pastras, T. Souflas, K. Tzimanis, H. Bikas, A computationally efficient multi-scale thermal modelling approach for PBF-LB/M based on the enthalpy method, Metals (Basel) 12 (2022), https://doi.org/10.3390/met12111853.
[99] C. Han, Y. Zou, Z. Dong, G. Hu, S. Xu, Y. Yang, D. Wang, Manipulating martensite transformation to achieve superior strength-ductility synergy in laser powder bed fusion of nickel-aluminium-bronze alloy via heat treatments, Virtual Phys Prototyp. 20 (2025) e2478227, https://doi.org/10.1080/17452759.2025.2478227.
[100] F. Meng, K.A. Liogas, K.B. Lau, Y. Deng, A.M. Korsunsky, P. Wang, X. Shen, C.H. T. Lee, The selection of scanning strategy and annealing schedule for the optimization of texture and magnetic properties of Fe-3.5 wt%Si alloy parts fabricated by laser powder bed fusion, Addit. Manuf. 97 (2025) 104614, https://doi.org/10.1016/j.addma.2024.104614.